
| | |
|---|---|
| Author: | **Benjamin Cheymol** |
| Reviewer: | |
| Date: | September 23, 2016 |
| Version: | 1.0 |
| ESS report number: | ESS-0068702 |

# Wire scanner scintillator

# Contents

**Abstract**

In the ESS linac [1], during commissioning and restart phase, wire scanner (WS) will be used intensively to characterize the transverse beam profiles. At low energy, the mode of detection is based on Secondary Emission (SE), while at energies above 200 MeV, the primary mode of detection will be the measurement of the hadronic shower created in the thin wire.

In this note we will present the design and the output signal estimation of the shower detector, based of inorganic crystal and silicon photodetector as well as the influence of beam losses on the measurement.

# Part I
# Signal level

## 1 Introduction

Wire scanners have been deployed successfully since decade in accelerator, they represent a conservative choice for beam profile measurement. Their principle is rather simple and consists of moving a wire across the beam while monitoring a signal proportional to the number of particles interacting with the beam, see Fig. 1. The signal observed is usually either the secondary emission current (SEM) from the wire, or the flux of high-energy secondary particles downstream of the wire. The high-energy secondaries are often detected with scintillators coupled to photomultiplier tubes (PMT).

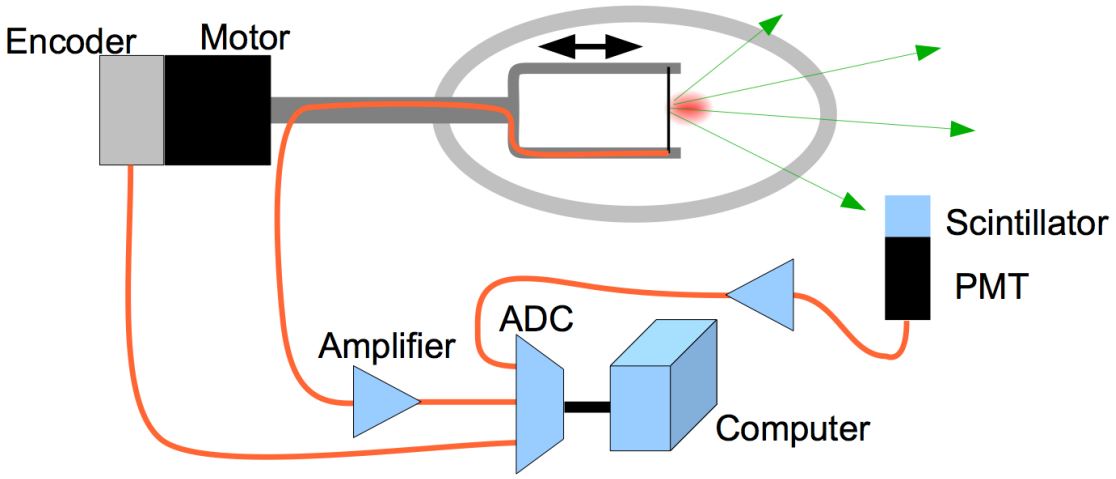


Figure 1: A thin wire is scanned through the particle beam while the secondary emission current, the signal from a calorimeter downstream, and the signal of the motor encoder are acquired simultaneously. Plotting either of the SEM or PMT signals against the encoder gives the beam profile.

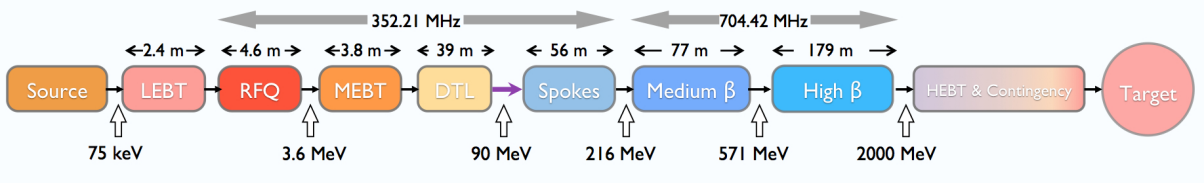


Figure 2: The layout of the ESS accelerator complex.

In the ESS superconducting linac and downstream (see Fig. 2), 8 WS stations will be installed along the beam line. Each station will be equipped with two linear actuator to sample the separately the transverse planes and the last 5 stations, in the elliptical

sections and in the transfer line to the target, will be used in shower detection mode in addition of the SE signal from the wire. The actuator fork will be equipped with a 40 $\mu m$ tungsten wire, for the ones to be used in the shower mode, the detectors will be positioned 400 mm downstream the wire.

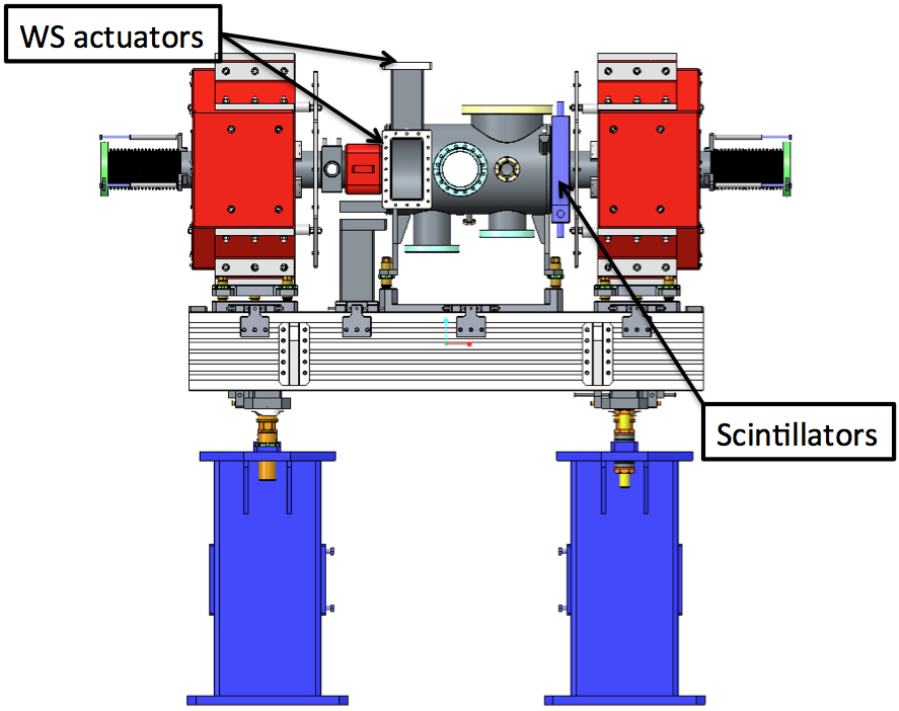


Figure 3: Preliminary design of the elliptical LWU, the total length flange to flange is ≈ 1932 mm, WS actuators are not shown (courtesy of STFC Daresbury Laboratory).

As shown in Fig. 3, due to the low energy of beam compared to proton synchrotron, the full system will be installed in a Linac Warm Unit (LWU), between two quadrupoles. This geometry has been chosen in order to avoid perturbation of the hadronic shower if the detectors would have been installed downstream the quadruple. Previous simulations show that 4 separated detector are needed to insure good homogeneity of the signal across the beam pipe [2], each detector will be connected to 2 Front-End (FE) electronic as for the SEM mode. The assembly geometry of the detector is shown in Fig. 4.

# 2 Detector concept

In high energy physics experiment, wavelength shifting (WLS) fibers are often used to collect the light from scintillator in order to reduce calorimeter geometry complexity [3]. The same approach can be use for the ESS wire scanner, not to simplify the geometry but to protect the photodetector from radiation.

The light generated in the scintillator can be collected through a fiber and then transported to the photodetector installed in an area with less radiation compare to the accelerator tunnel. In an ideal case, the photodetector can be installed in the klystron gallery in the same electronic cabinet as its front end electronic and its digitizer card.

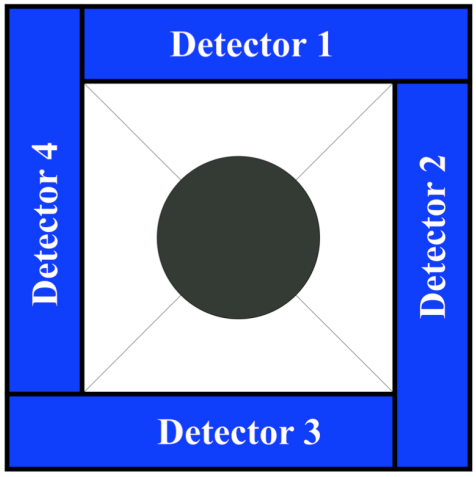


Figure 4: Detector assembly for the ESS WS system.

## 2.1 Light collection with WLS fiber

The WLS fiber consist in a polystyrene core (n=1.6) surrounding by single or double acrylic cladding (n=1.49 for the inner clad, n=1.42 for the outer clad). The fibers are available in different diameter form 0.2 mm to 2 mm. The cladding material is highly transparent to the incoming scintillation light, while the core has a short absorption length ($\approx 0.1\ mm$) at the peak absorption. The absorbed light is then remitted isotropically to longer wavelength, typically, the blue light is shifted to green as shown in Fig 5.

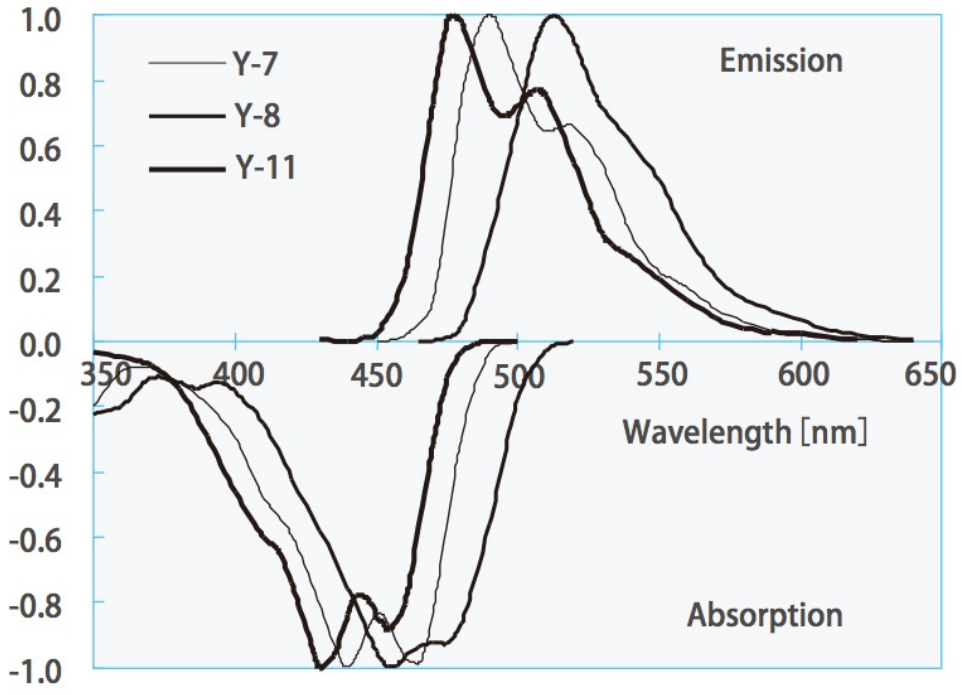


Figure 5: Absorption and emission spectra of various WLS from Kuraray.

The trapping efficiency of the light is $\approx 3$ % for a single clan fiber and $\approx 5.6$ % for a

double clad fiber, which correspond to a numerical aperture of 0.58 and 0.74 respectively. The absorption length of the fiber at their peak emission is about few meters depending to the type and composition of the fiber core, the length must be kept short to avoid too high light losses.

In general the WLS fibers are installed in groove machined directly on the scintillator, the groove is filled optical glue/grease to improve the coupling between the different elements. The geometry of the fiber as well as the geometry of the scintillator have a strong impact on the light collection yield, this yield can be improved by using multiple fibers or multiple fiber loops as shown in Fig. 6 for exemple.

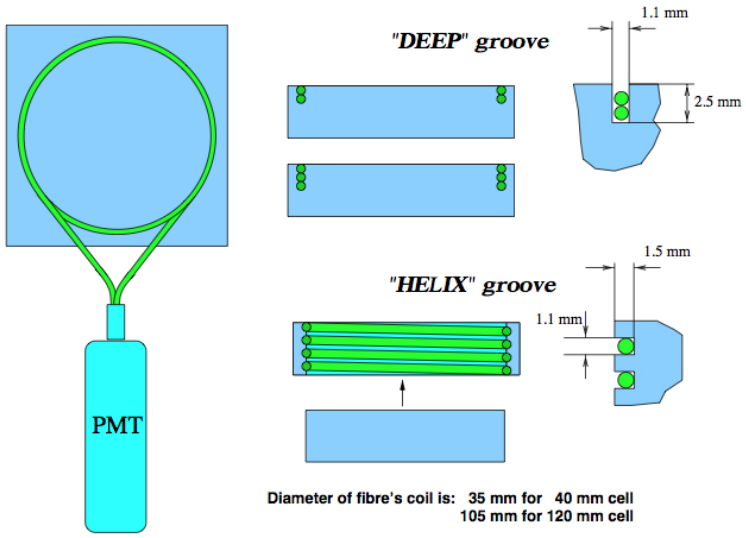


Figure 1: Design of preshower prototypes.

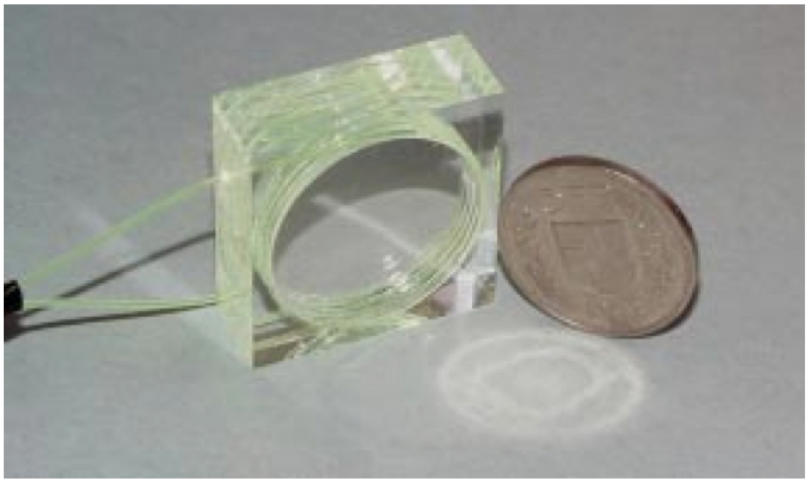

Figure 6: LHCb preshower scintillator design [3].

visite

## 2.2 Detector architecture

The acquisition electronic of the ESS WS is currently under development at Synchrotrone Elettra Trieste. For the SEM mode, it is foreseen to use two separated channels per wire, one with high gain and low bandwidth the other with a low gain and high bandwidth. With this setup it will possible to get a high dynamic range for the profile in a single scan. The same concept will be used for the scintillator readout.

A combination of WLS fiber and clear fiber will be used to transport the light from the detector to a radiation free area, the detector architecture is shown in Fig. 7.

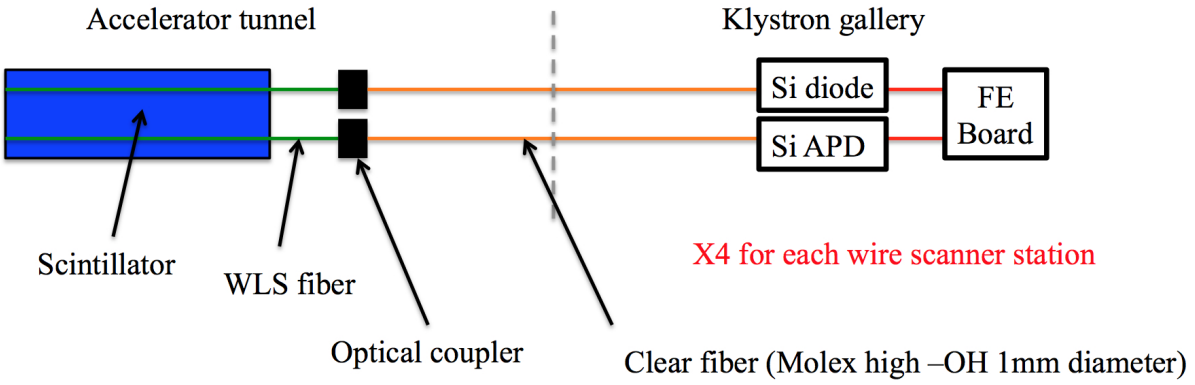


Figure 7: Conceptual design of the ESS wire scanner shower detector.

The scintillation light will be collected by two WLS fiber on each detector assembly, for the ESS application the length from the WS station in the tunnel to the electronic rack in the klystron gallery is about 60 meters, since the short attenuation length of this fiber, their lengths have to be kept as short as possible. Silica fiber have a lower attenuations, and are better candidates to transport the light over a long distance,

The light will be converted to current by a photodiode and an avalanche photodiode, in order to increase the dynamic range of the measurement. Each photodetector will be connected to its own FE electronic and digitizer.

## 2.3 Scintillator and WLS choice

Most of the plastic and crystal scintillator have their peak emission in the visible range of the light, more precisely in the blue-green region. WLS can be used to shift the blue light to green light, their absorption peak shall match the peak emission of the scintillator, the BCF-91a from Saint Gobain and the Y-11 from Kuraray have a peak absorption close to 420 nm, which corresponds to the peak emission of the majority of plastic scintillator. Unfortunately, the radiation dose in the accelerator tunnel might be too high for organic scintillator, crystals are less sensitive to radiation and seems a better option.

One alternative to plastic scintillator is to use the LSO scintillator, which had a peak emission at 420 nm, a fast decay time (40 ns) and a high photon yield ($\approx$ 30 $\gamma$ .keV$^{-1}$), in addition, the LSO is not hydroscopic unlike the NaI crystal. The LSO has been study extensively for calorimetry application for high energy physics and is available from different supplier [4].

As show in Fig. 8, its spectra matches the two WLS fibers considered, 80 % of the spectra are absorbed, only the high wavelengths are outside the absorption spectra of the fibers.

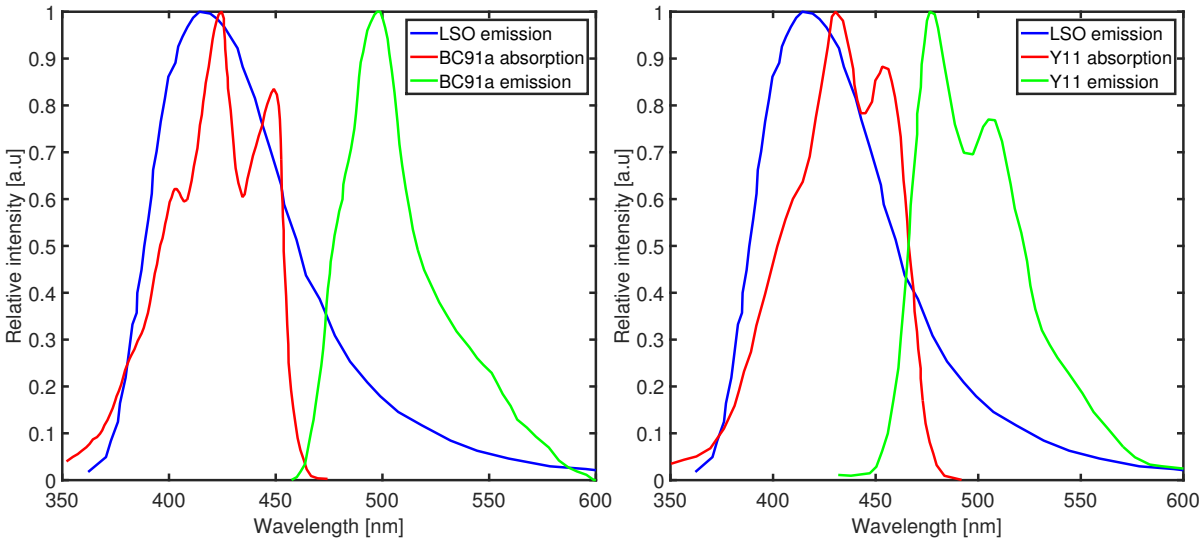


Figure 8: Optical spectra of the Saint Gobain BCF-91A and the Kuraray Y11 wavelength shifter.

In order to match the numerical aperture ($NA$) of a silica fiber and its diameter, a 1 mm diameter single clad fiber has been considered . The decay time of such fibers is few ns.

# 3 Simulations of the detector

The light production and collection have been simulated by the Monte Carlo (MC) code FLUKA [5], the shifting process, the light transport have been treated analytically in post processing. The detector assembly geometry used in the MC simulations is shown in Fig 9.

The crystal might be difficult to machine, therefore, a plastic light guide (Saint Gobain BC-800, $n = 1.49$) will be used to installed the WLS fiber in groove filled with optical glue ($n = 1.56$), the detector size is $250 \times 45 \times 30mm^3$, the light guide dimension is $250 \times 5 \times 30mm^3$. All the assembly in surrounded by reflecting material, with a reflexion varying index from 0.94 to 0.99 and encapsulated in an aluminum box with a thickness of 2 mm. The WLS fiber has been simulated as a cylinder of 1 mm diameter for the core surrounding with a 20 $\mu m$ thick clad, materials are polystyrene for the core and PMMA for the clad.

In addition, for an upgrade phase of the WS system, a Cherenkov radiator (in quartz) will be installed in front of the scintillator assembly. Bremsstrahlung background from the cavities might perturb the profile measurement, a Cherenkov detector is insensitive to this radiation and should allow beam profile measurement when the cavities are at their

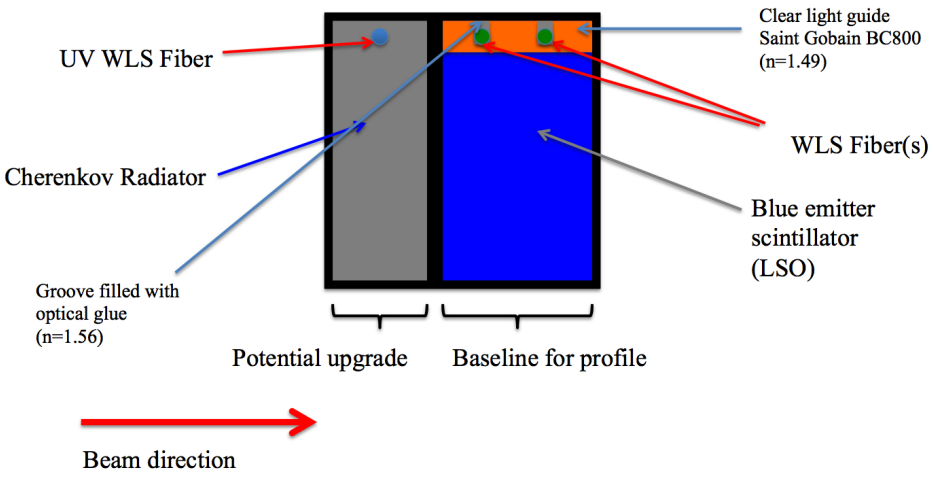


Figure 9: Cross section of the detector assembly used in the MC simulations.

peak accelerating gradient. A similar detector architecture is foreseen for the Cherenkov detector with an UV WLS fiber [6].

## 3.1 Particle flux

The particle fluence for different beam energy (from 220 MeV to 2 GeV) has been measured with the MC code. The hadronic shower is dominated by protons, pions, neutrons, gamma, elections and positron, thus only these particles type have been measured.

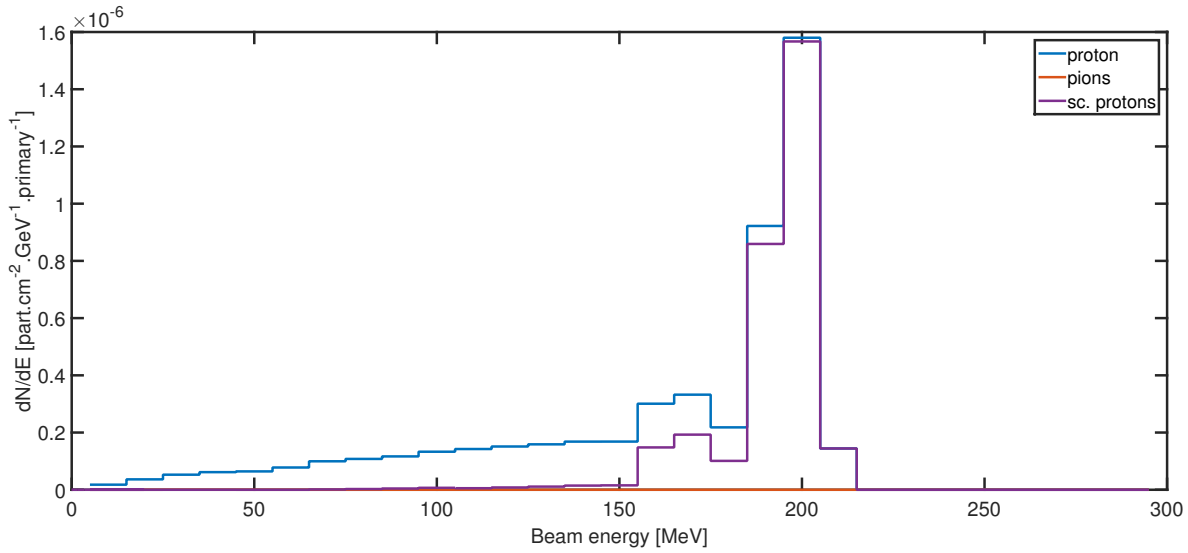


Figure 10: Protons and pions spectra on the detector surface for a beam energy equal to 220 MeV.

As shown in Fig. 10 to Fig. 13, the hadronic shower is dominated by neutral particles, in particular for the low energy part of the spectra. It is interesting to note that close to

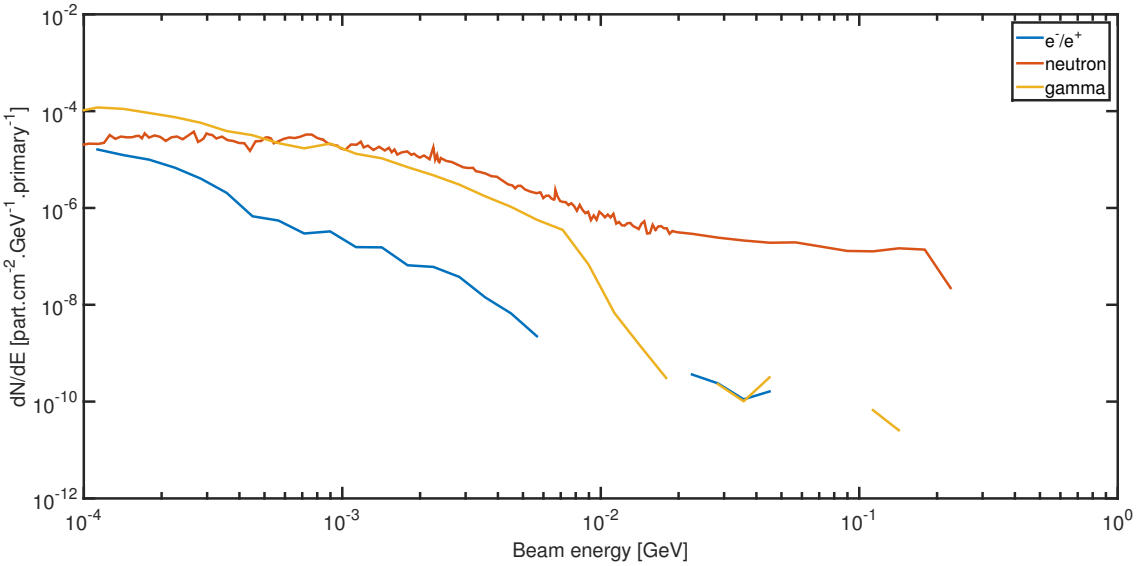


Figure 11: Neutron, gamma, election and positron spectra on the detector surface for a beam energy equal to 220 MeV.

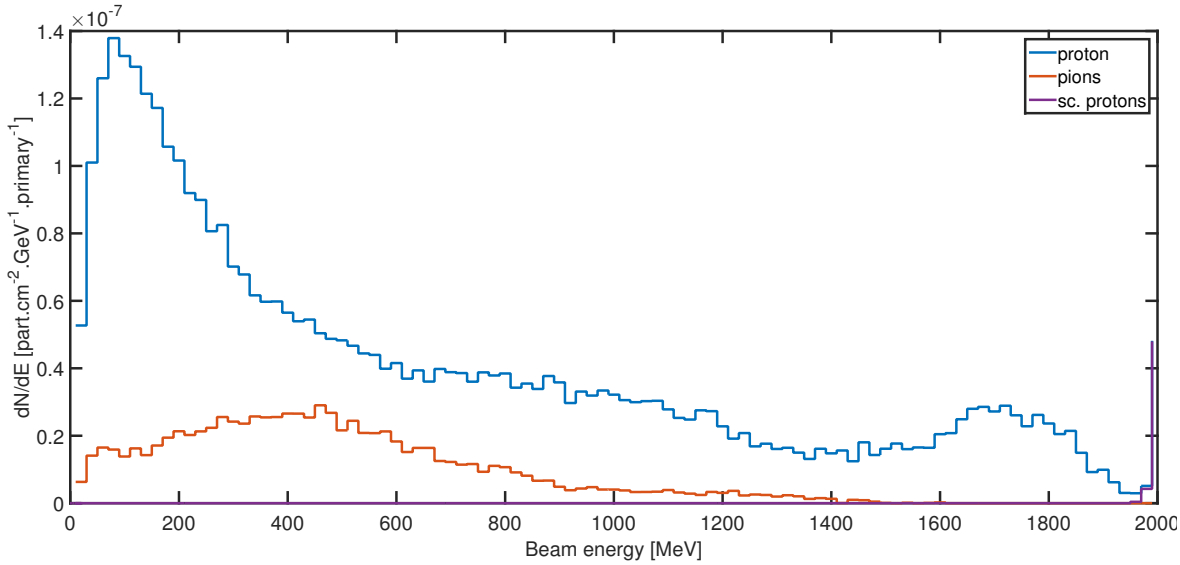


Figure 12: Protons and pions on the detector surface for a beam energy equal to 2000 MeV.

the beam energy, the protons are dominant and a peak can be seen on the spectra with energy almost equal to the beam energy. The spectra from beam energies equal to 570 MeV, 1000 MeV, 1300 MeV, 1500 MeV and 2000 MeV are presented in annex.

## 3.2 Deposited energy

In a first approximation, the signal of the scintillator is proportional to the deposited energy. The contribution to the signal of the main particles of the shower has been measured for various beam energies.

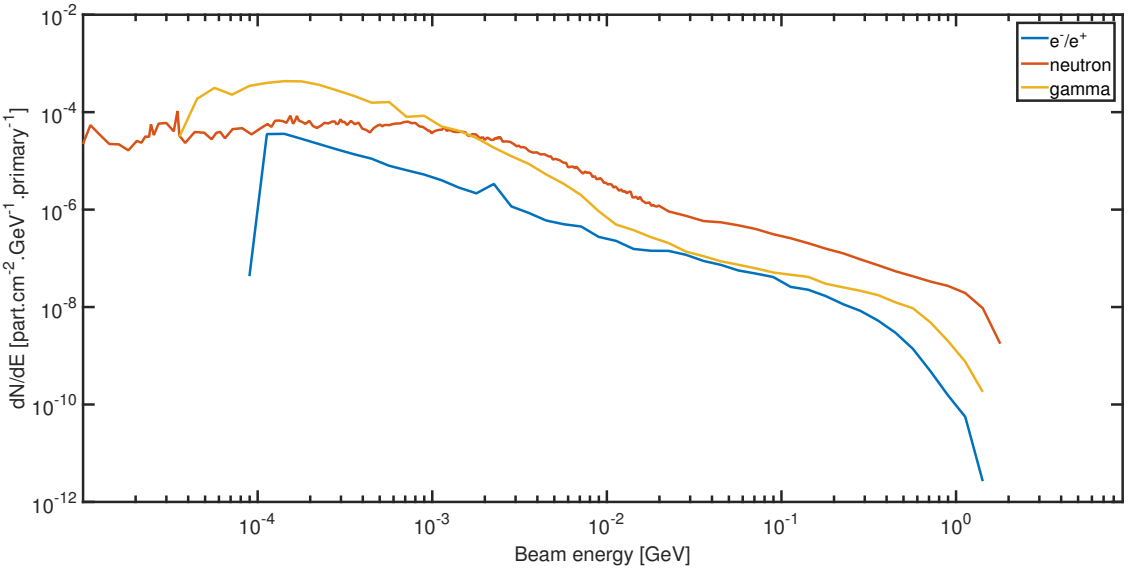


Figure 13: Neutron, gamma, election and positron spectra on the detector surface for a beam energy equal to 2000 MeV.

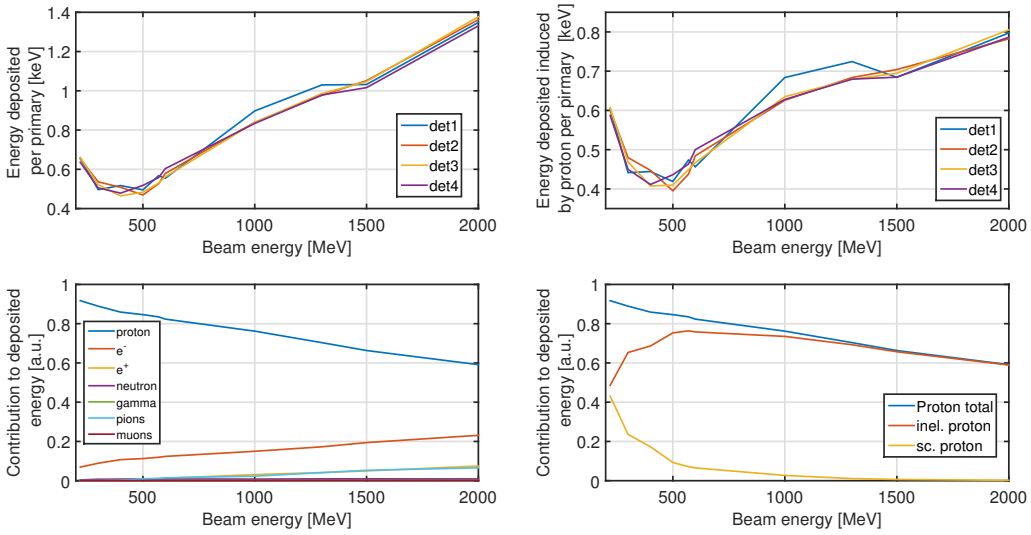


Figure 14: The 2 upper lot are presenting the total energy deposition (left) and the energy deposition induced by protons (right) for the 4 scintillators. In the bottom. the plot in the left is summarizing the contribution of the main particles type to the deposited energy, on the right, the plot is summering the contribution of the protons.

As show in Fig. 14, the signal is dominated by the contribution of the charge particles considered in the measurement $(p, e^-, e^+, \pi^{+/-}, \mu^{+/-})$, their contribution is above 96 % of the signal. The contribution of the proton is dominant at for all the beam energies from 90 % at 220 MeV to 60 % at 2000 MeV. For this particular type of particle, for the lowest energy considered, the contribution of beam scattered particles and proton from inelastic reaction are almost equal. When the beam energy increases the contribution to

the signal of the scattered protons decreases rapidly, while up to 600 MeV the energy deposited per inelastic protons increases very slowly (see Fig. 15).

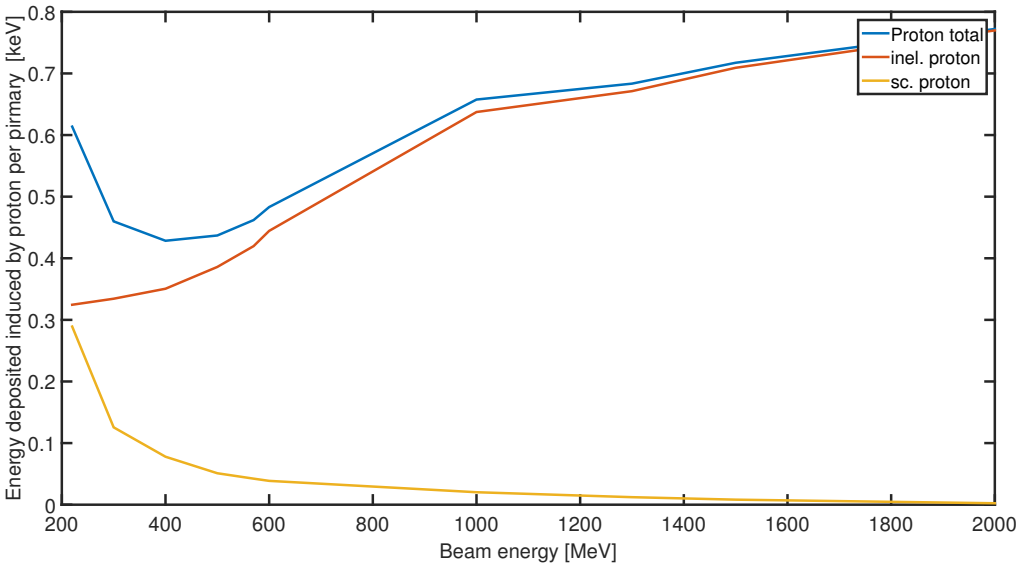


Figure 15: Energy deposition in a scintillator fro elastic and inelastic protons as function of the beam energy.

For the geometry considered, the scattered protons are stopped in the scintillator material fore beam energy up to 170-180 MeV, above this threshold, the energy deposited is decreasing with the energy and the number of scattered protons is decreasing as well. The combination of these 2 effects can explain the local minima on the curve in Fig. 14, the rapid decrease of the signal induced by scattered particles is not compensated by the signal generated by secondaries particles.

## 3.3 Light collection and transport

The light production and the absorption by the WLS fiber have been simulated with a simplified geometry. In the MC code, only one scintillator assembly has been simulated with a beam interacting directly with the detector. The number of photons generated in the crystal and the number of photons absorbed in the WLS fiber core have been measured for different reflective material index and separately on both fibers. The results show that light collection yield per fiber varies from 9 % to 14 % as function of the reflective index (see Fig. 16). Note that the light collection yield is identical for both fiber, thus for given wire position the light power at the exit of the 2 fiber will be identical.

The conversion in the WLS fiber and the light transport has been calculated in post processing. In the MC code, the scintillation light is monochromatic, a coefficient equal 0.8 has been applied to simulate the non absorption of the high energy wavelength of the LSO spectrum. In addition a the WLS quantum efficiency of the WLS fiber is set at 0.85, and the light trapping efficiency to 0.03.

The last parameter might be increased if the fiber end is wrapped by a reflecting material, in the simulation presented in this note, it is assumed that the light is not

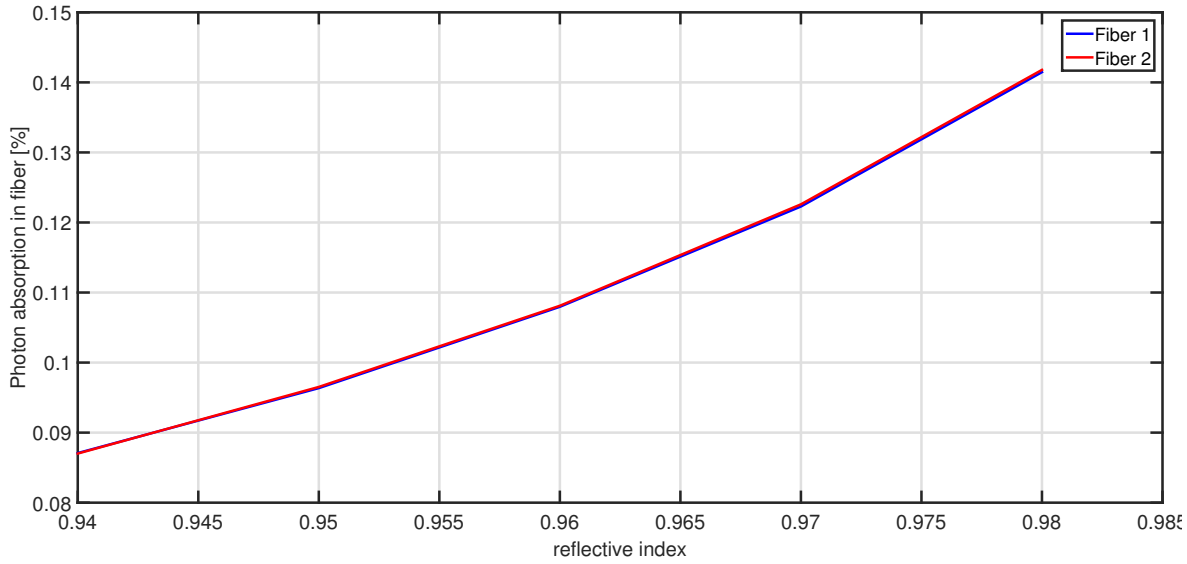


Figure 16: Proportion of scintillation photon absorbed in the 2 WLS fibers as function of wrapping material reflective index.

reflected and thus lost. Note that the trapping efficiency can go up to $\approx 0.05 - 0.06$ if the light is fully reflected on the fiber end.

As mentioned previously, the WLS fibers have a short attenuation length, clear plastic fiber have also a short length for our application and are radiation sensitive. Silica fibers have long attenuation length and are less sensitive to radiation, two options have been estimated:

- A pure Silica fiber ($NA \approx$ 0.22)
- A silica fiber with hard polymer cladding (SPC) ($NA \approx$ 0.48)

Both have attenuation equal to $\approx$ 25 dB.km$^{-1}$ at the peak emission of the WLS fiber (500 nm). The pure silica fiber has a higher resistance to radiation, but a low $NA$ compare to the WLS fiber ($NA \approx$ 0.5), only 40 % of the light from the WLS fiver can be trapped in the silica fiber, in addition the optical connector has an efficiency of 80-90 %, in total the full efficiency of this system is about 30 %.

Due to the higher NA of the SPC fiber, up to 90 % of the light coming from the WLS fiber can be trapped and transport. Nevertheless the radiation resistance of this fiber is less, one possible mitigation is to split the clear fiber path in two. The first one from the detector to the tunnel penetration will allow easy maintenance and replacement of the exposed part of the fiber, the other, from the penetration to the klystron gallery. In this case the fiber will not exposed to high radiation dose and will be installed permanently in the cable tray. Two optical connectors are needed for the solution, assuming he same efficiency of $\approx$ 85 %, the proportion of the light transported is up to 60 %.

The two options have been considered for the signal estimation. In addition, the light transport on a clear plastic fiber have simulated, with the same optical connector efficiency and an attenuation equal to $\approx$ 100 dB.km$^{-1}$.

## 3.4 Signal estimation

For this simulation, a simplified geometry of the LWU has been modeled in the MC code, the wire consists in a foil with a thickness equal to 32 $\mu m$ to take in account the round shape of the wire, the energy deposited in each scintillator has been measured and then use as input for post processing. In the first step, the number of photons generated per proton crossing the wire (in the center of the beam pipe) has been estimated for beam energy from 100 MeV to 2100 MeV by converting the deposited energy in photon (see Fig. 17).

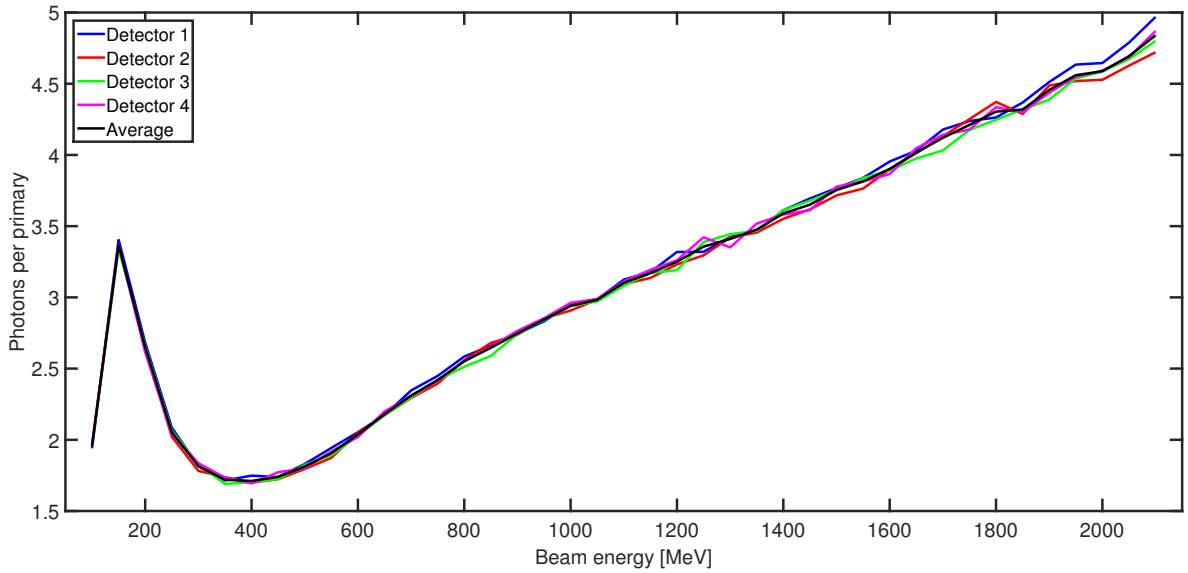


Figure 17: Number of photons generated in the LSO crystals per proton crossing the wire as function of the beam energy.

The response of the 4 scintillators is almost equal, an average value has been taken for the next steps of the study. The minimum signal is expected for a beam energy equal to 400 MeV, above this energy, the signal increase almost linearly with the beam energy. A peak can be seen at 150 MeV, corresponding to a full energy deposition of scattered proton in the detector.

These data have been then used to estimate the peak light power at 400 and 2000 MeV as function of a clear fiber length for the two options presented in the previous section. In this estimation, the light collection efficiency of the WLS fiber is set to 11 % which correspond to a reflective index of the material equal to 0.96, the emission of the WLS is assumed to be monochromatic ($\lambda$=500 nm). The beam sizes are assumed to be equal to 2 mm in both transverse planes and the beam intensity is set to 62.5 mA.

As shown in Fig. 18 and Fig. 19, the light power varies by a factor 5 depending on the beam energy and on the efficiency of the clear fiber.

After 60 meters of clear fiber, the peak light power is a range from $\approx$ 15 W at 400 MeV with lowest fiber efficiency to $\approx$60 W at 2000 MeV and the highest fiber efficiency for a silica fiber (Fig. 18), and from $\approx$ 4 W to $\approx$ 19 W for a plastic clear fiber (Fig. 19).

The photodetectors shall have a high sensitivity at 500 nm, a surface larger than the section of the fiber to insure good optical coupling and a low noise, the Si diode S1227-

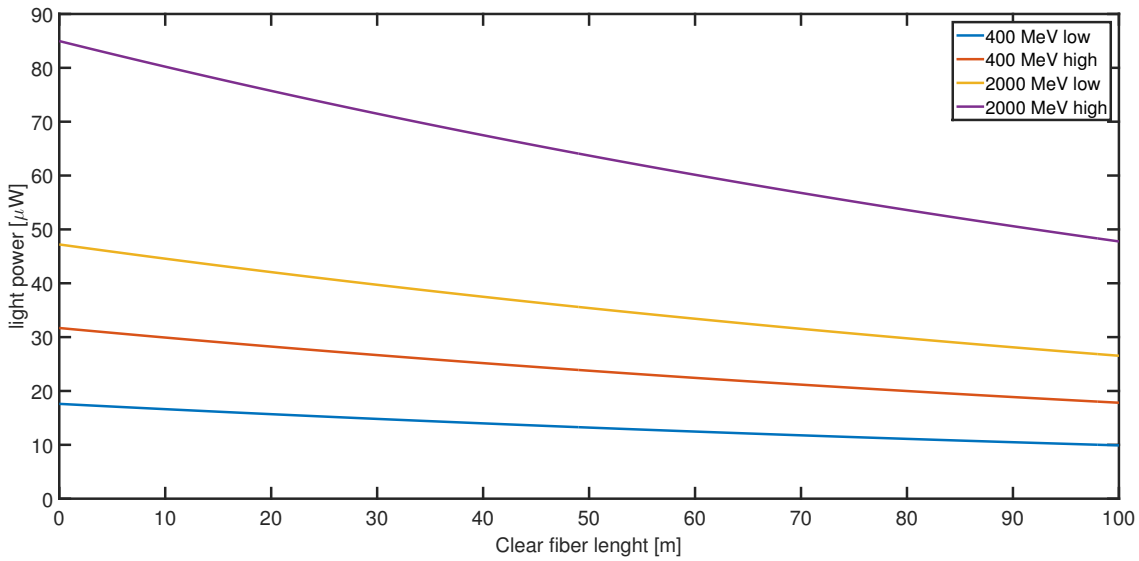


Figure 18: Peak light power as function of the clear silica fiber length for a beam energy equal to 400 and 2000 MeV. *low* corresponds to the efficiency of a pure silica fiber, *high* corresponds to the efficiency of a SPC fiber.

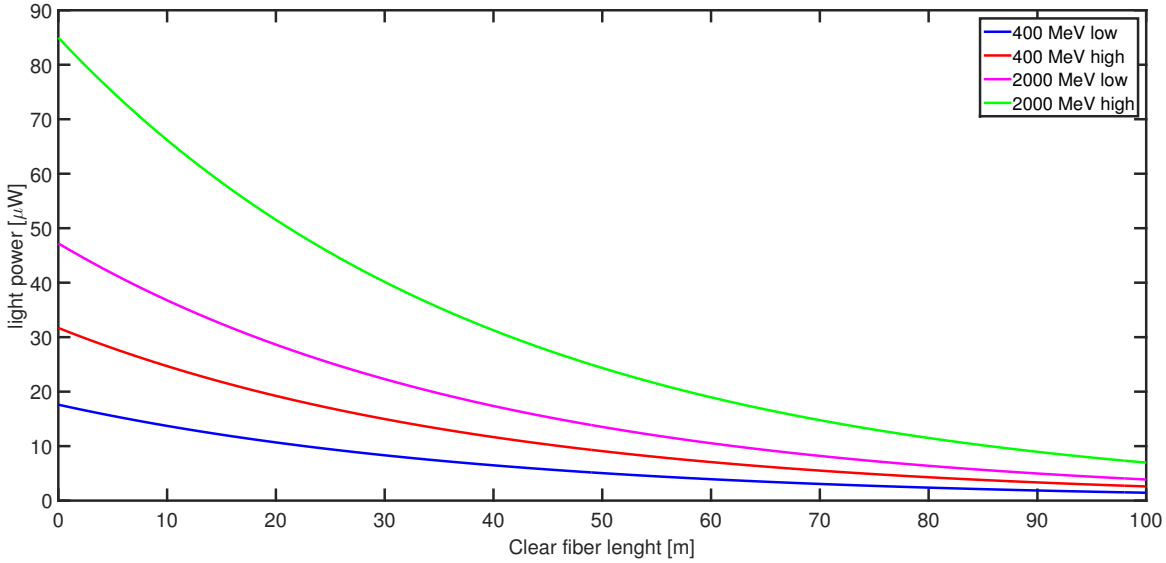


Figure 19: Peak light power as function of the clear plastic fiber length for a beam energy equal to 400 and 2000 MeV. *low* corresponds to optical connector(s) efficiency equal to 30 %, *high* corresponds to optical connector(s) efficiency equal to 60 %.

33BR and the APD S5344 from Hamamatsu fit these requirements and their sensitivity (0.3 A.W$^{-1}$ for the diode and 20 A.W$^{-1}$ for the APD) have use to estimate the signal, note that the gain of the APD is set at a constant value in the estimation and might be too high in some cases, saturation of the detector might perturb the measurement.

The expected signals as function of the wire position for both type of detectors and both type of fiber are shown in Fig. 20 and Fig. 21

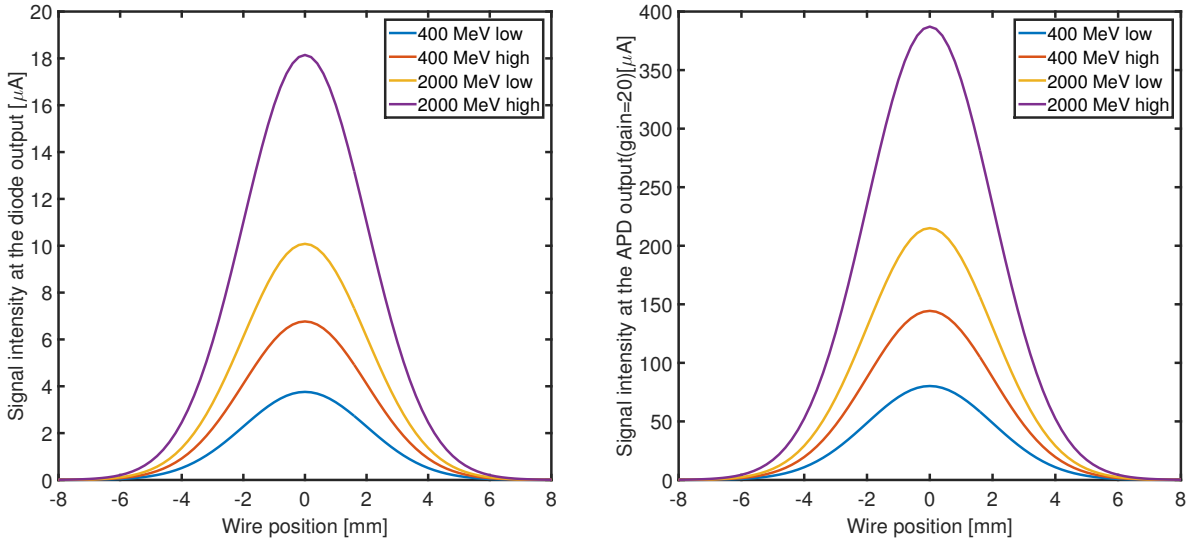


Figure 20: Expected signal at the output of the Si diode (right) and APD (left) after 60 m of clear silica fiber.

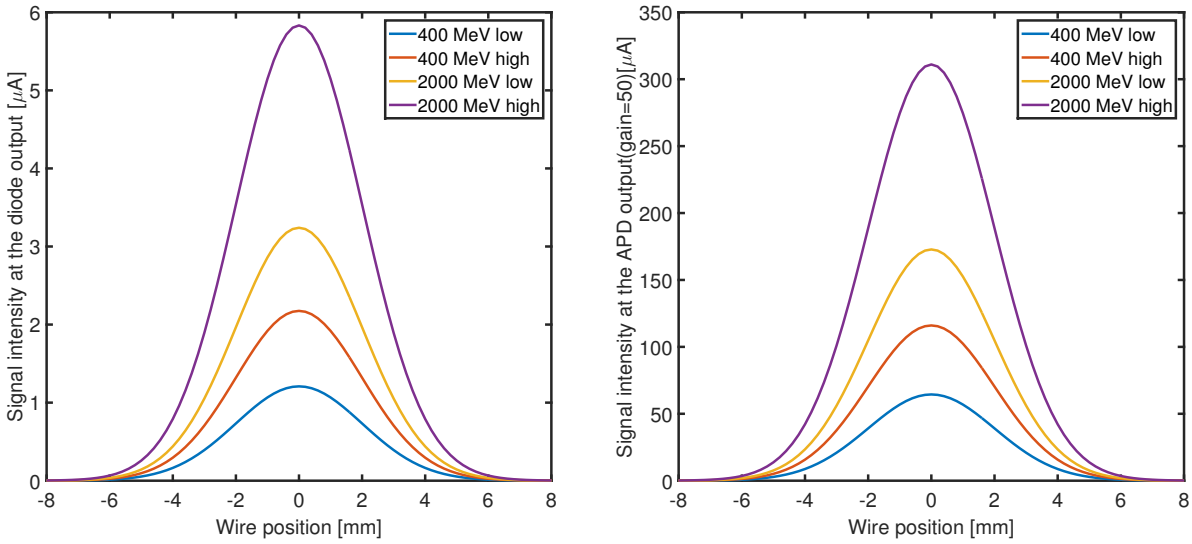


Figure 21: Expected signal at the output of the Si diode (right) and APD (left) after 60 m of clear plastic fiber).

All these inputs are used as inputs for the FE specifications, after the preliminary design phase, the choice of the photodetector will be frozen.

## 3.5 Time dependency of the signal

A bunch by bunch measurement of the profile like in the synchrotron is not mandatory for a linac application, a time resolution of 0.5-1 $\mu s$ is requested for the ESS WS system. The decay time of the detector assembly is long compare to the bunch frequency of the ESS linac (2.86 ns), the bunch structure will be vanished but some artifact might appear,

simulations have been performed to cheek this effect.

In a first approximation, it was assumed that the bunch length (up to 20 ps) is null compare to the LSO crystal decay time, the charge per bunch is identical and the wire is not moving. The arrival time of the scintillation photon on the WLS fibber has been measured with the MC code, the decay time of the fiber and the different optical path of the shifted photon have been simulated in post processing for a single bunch. The time distribution obtained has been used to generate the time structure of the signal at the exit of the WLS fiber, by shifting the original distribution by 2.86 ns and adding the the new distribution to the previous distribution.

As shown in Fig. 22 for a beam pulse equal to 5 $\mu s$, the expected signal will have a rise and decay time equal to ≈300 ns, on the flat top on the signal the signal is almost constant (¡ 1 % peak to peak) and shows a time structure with a frequency equal to 352 MHz.

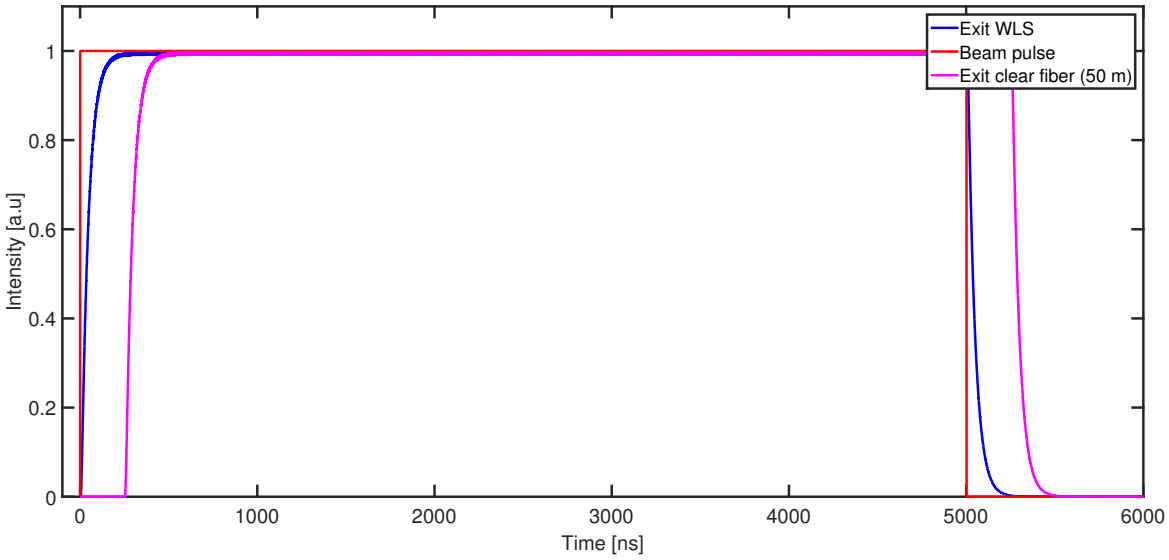


Figure 22: Expected rise/fall time signal for (i.e light) a single wire position, beam pulse is 5 $\mu s$.

After 50 meters of clear fiber, the signal will be shifted by 250 ns, it was assumed that the silica fibers are not inducing time dispersion.

## 3.6 Detector homogeneity

The homogeneity response of the detectors has been checked with same MC code, a pencil beam is moved across the beam pipe aperture form -25 mm to 25 mm in step of 5 mm, and then interacts with the tungsten foil, the energy deposited in each scintillators has been measured, it is assumed that the signal will be proportional to this quantity.

As shown in Fig. 23 and Fig. 24, the signal can vary increase by almost 50 % across the beam pipe aperture if a single detector is installed. 4 detectors are needed to insure a good homogeneity. At 2000 MeV by summing the signal from the 4 detectors the absolute error is less than 2 % over the range considered in the study (see Fig. 25 and Fig. 26) , it has to be noted that the error is close to the statistical error of the MC code.

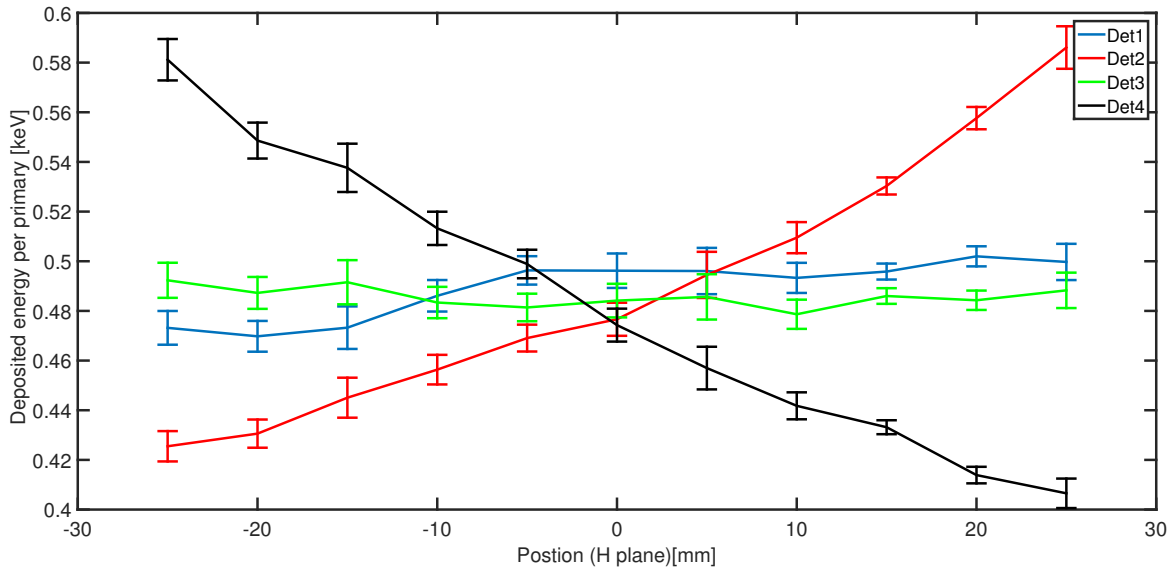


Figure 23: Energy deposited in each of the detectors at y=0 when the horizontal plane is scanned, beam energy is 400 MeV. Similar results are observed in the vertical plane with an inversion of the detector curves (i.e the flat curves are obtained with detector 2 and 4)

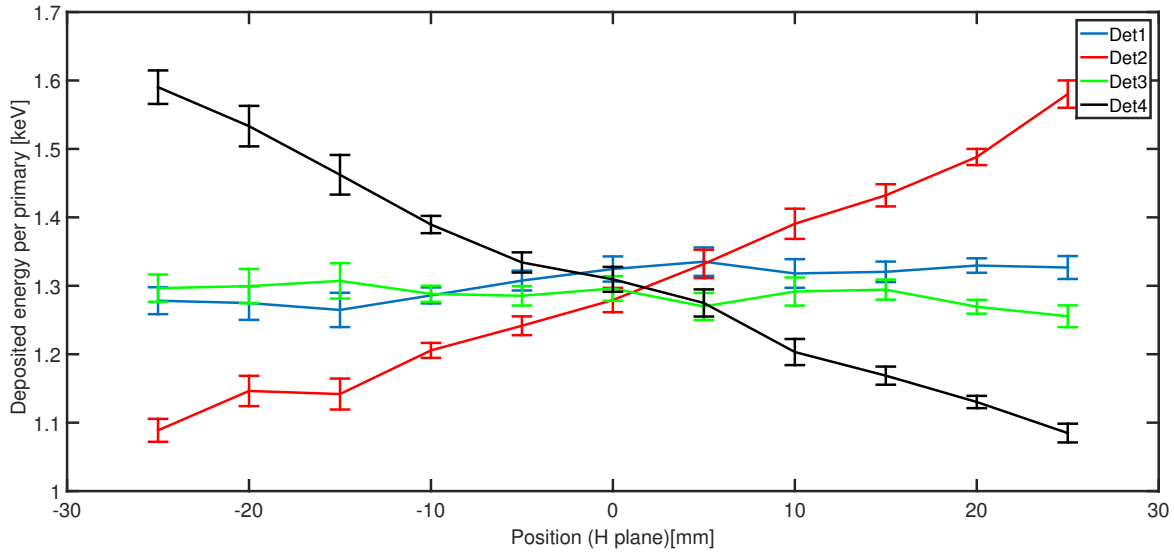


Figure 24: Energy deposited in each of the detectors at y=0 when the horizontal plane is scanned beam energy is 2000 MeV. Similar results are observed in the vertical plane with an inversion of the detector curves (i.e the flat curves are obtained with detector 2 and 4)

# 4 Preliminary estimation of the Cherenkov signal

A series of simple MC simulations have been performed to estimate the expected signal level generated by the Cherenkov radiator. it would interesting to use a similar concept as the scintillator readout in order to avoid electronic in the tunnel. Most of the simu-

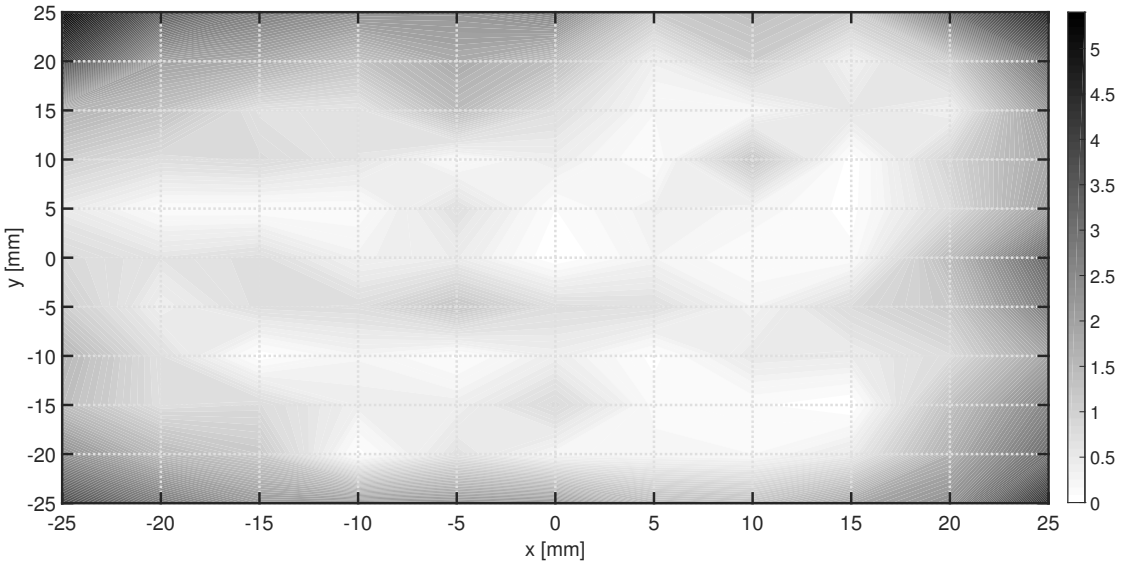


Figure 25: Absolute error map as function of the wire position, the beam energy is equal to 400 MeV.

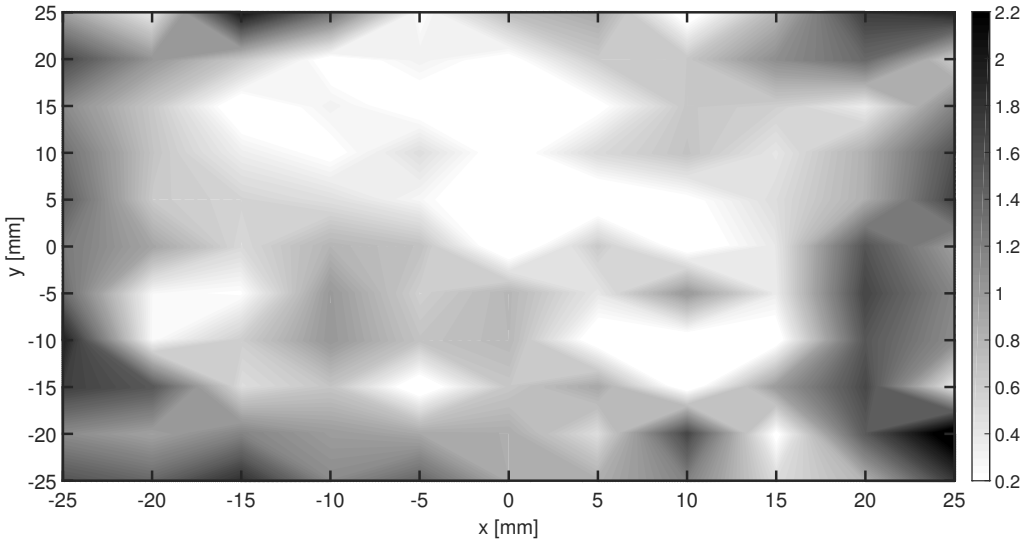


Figure 26: Absolute error map as function of the wire position, the beam energy is equal to 2000 MeV.

lations and post processing are identical, at the exception of the WLS fiber and of the photodetector.

The spectra of the Cherenkov is in $1/\lambda^2$ and the Saint Gobain BCF-92 has a peak absorption close to 400 nm, the absorption is also higher for shorter wavelength compare to the BCF-91a or Y-11 fibers. In the MC simulation, only the Cherenkov photon from 350 to 450 nm have been generated to match the absorption spectra of the BCF-92 fiber.

The light yield of the Cherenkov radiation is 3 or 4 orders of magnitude less than the light yield of common scintillator. The signal at the exit of the an APD or a Si diode

might be too low, for this application a PMT seems a better option. In pot-processing, the sensitivity of the PMT was set to $5.10^4 A.W^{-1}$. For This simulations, only the case of clear plastic fiber has been simulated.

## 4.1 Cherenkov radiator

4 different radiator have been simulated:

- A silicate aerogel ($n = 1.06$).
- Quartz ($n = 1.46$).
- The BC484 plastic ($n = 1.58$).
- A heavy glass ($n = 1.75$).

These radiators have a different energy threshold, it might be possible to match the threshold energy of the detector to the beam energy to reduce the background.

The BC484 from Saint Gobain is a WLS with a peak absorption at 376 nm and a peak emission of 428 nm (see Fig. 27), which matches the peak absorption of the BCF-91A. Since the Cherenkov light between ≈300 nm and ≈425 nm will be almost immediately absorbed and reemitted isotropically at a wavelength between ≈400 nn and ≈550 nm, the repose of the BC484 will be similar to a plastic scintillator. Moreover, the WLS fiber can be directly mounted on the radiator and thus will improve the light collection efficiency. For the other radiators, a clear guide must be used to insert the WLS fiber, in a first step, the same materials as for the scintillation detector have been used.

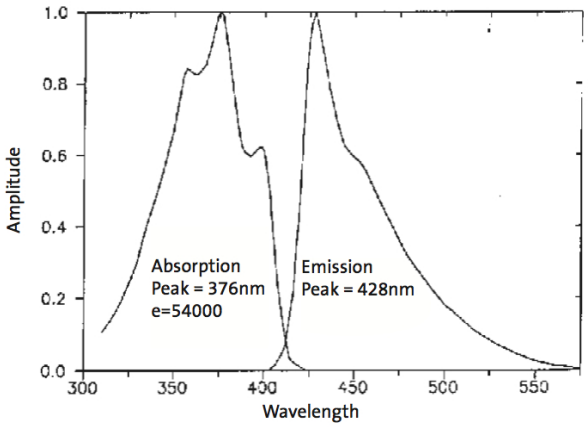


Figure 27: Optical spectra of the Saint Gobain BC484 wavelength shifter.

## 4.2 Signal estimation

For this estimation, a single detector have been implemented in the MC code, the LWU is also simplified compare to the geometry used in the estimation of the scintillation light. The beam entry was set in a range from 200 MeV to 2 GeV in step of 100 MeV. For the

BC484 case, the number of Cherenkov photon between 350 nm and 450 nm have been scored, in post processing, it was assumed that all the photons were shifted, that the light collection efficnice on the fiber was 21 % (see Fig. 33) and 85 % of the photon reaching the fiber were absorbed. For the other radiators, the number of Cherenkov photons absorbed in the WLS were scored. For all the cases, the trapping efficiency of the WLS fiber was 0.03. Not that the number of primary particles is low in these simulations and the statistical error is comprised between 5 and 10 %.

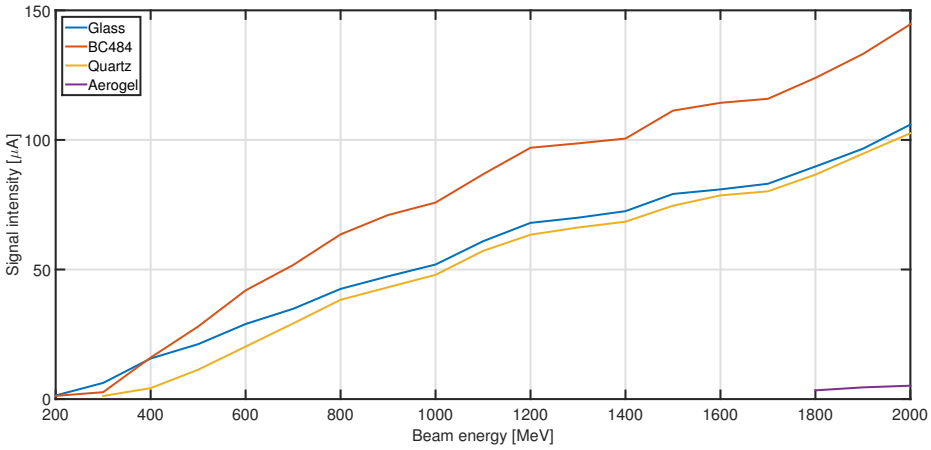


Figure 28: Expected peak Cherenkov signal for different radiators as function of the beam energy. The efficiency of the optical coupling of the fibers is 60 %, the length of the plastic fiber is set to 60 meters.

In the High $\beta$ section (i.e. above $\approx$ 600 MeV), the Cherenkov light might be a good alternative to the scintillation light with an expected signal from $\approx$ 10 $\mu A$ to $\approx$ 150 $\mu A$ depending on the beam energy and on the radiator. At lower energy, the signal is too weak to insure good beam profile reconstruction, the light collection shall be improved, one possible solution might be to connecte the photodetector directly to the radiator.

The studies will continue in the following months, in particular in order to:

- Optimize the signal at low energy.
- Optimize the light collection in order to measure the beam halo.
- Check the homogeneity of the detector.

# 5 Alternative design

The cost of LSO crystal might be too high, therefore we propose to study a cheaper alternative based on plastic scintillator, despite its higher sensitivity to radiation damage. The light power of the new geometry shall be comparable to the one presented in the previous section to keep the same parameters for the FE.

## 5.1 Detector geometry

Changing the inorganic crystal to BC408 plastic scintillator with the same geometry (including the clear light guide) will reduce the light power by approximately a factor 20. To keep a similar beam power, the geometry must be changed. The size of the scintillator can be increased and the WLS fiber geometry changed. Due to space restriction in the LWU, the thickness can not exceed 50 mm, the transverse dimensions are less constraint and can be increase by almost a factor 2 to capture more secondaries particles, in the MC simulations, the sector size is equal to $300 \times 100 \times 50\ mm$, the volume of this new detector is 4 times bigger than the LSO crystal.

With a larger size, the WLS fiber position can be optimized, a geometry for the fiber is similar to the one shown in Fig. 6 can implemented in the detector. The fiber can make a loop on one of the 2 largest face of the scintillator resulting in an Hyppodrome-like shape, the large radius of the geometry will limit the light losses [1].

A preliminary estimation of the light collection efficiency have been perform, assuming a 1 mm diameter WLS fiber, arranged in a single loop in the machined grooved filled with optical glue.

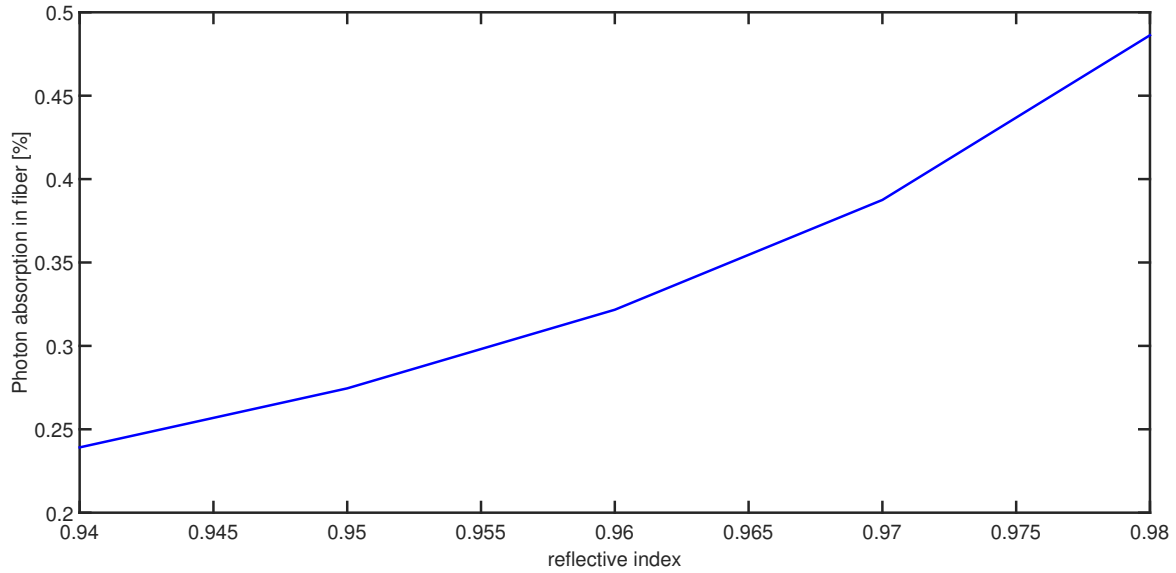


Figure 29: Light collection efficiency of the plastic based detector as function of the reflective index of the wrapping material.

As shown in Fig. 29, the light collection efficiency is almost a factor 4 higher than the geometry presented in Fig 9 [2]. Moreover, since the shifted photon will be transported along both direction of the fiber, with this geometry the light can be collected from both fiber end, then transport and measured with the 2 separated channel, the light power will be indentical on the 2 channels.

[1] The light loss induced by a 20 mm bending radius is $\approx 10$ %

[2] by a factor 2 if the contributions of the 2 fibers of the previous geometry are summed

## 5.2 Signal estimation

As for the LSO based detector, the light power as function to the clear fiber length has been estimated. The parameters used in post processing are identical.

As show in Fig. 30 for the case of a clear plastic fiber, the light power is ≈3 times less compare to the same set up with LSO crystal.

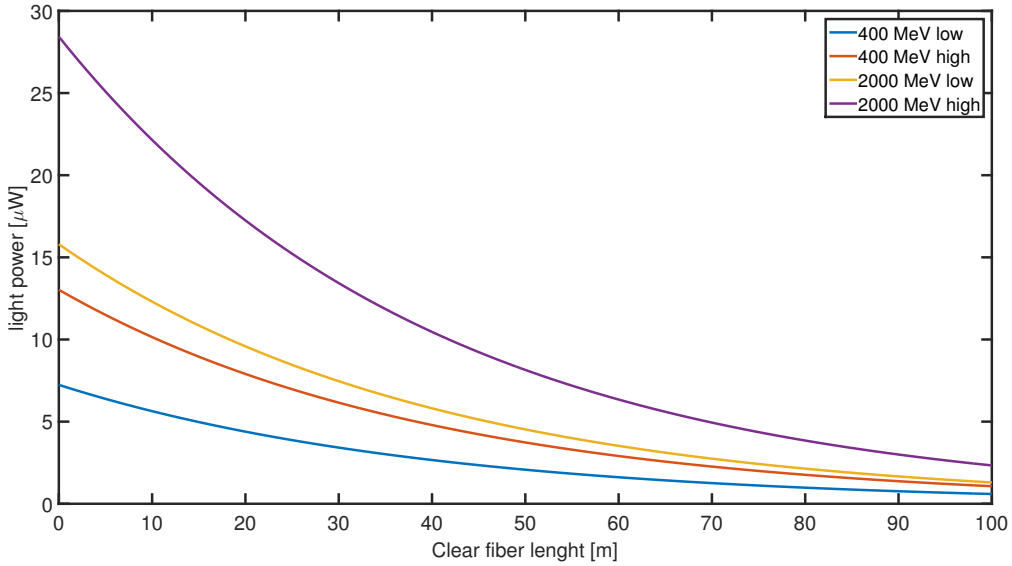


Figure 30: Light power as function of clear plastic fiber length.

Using silica fiber will improve the light transport, and in this case the expected signal is a little bit higher than the LSO based detector with clear plastic fiber.

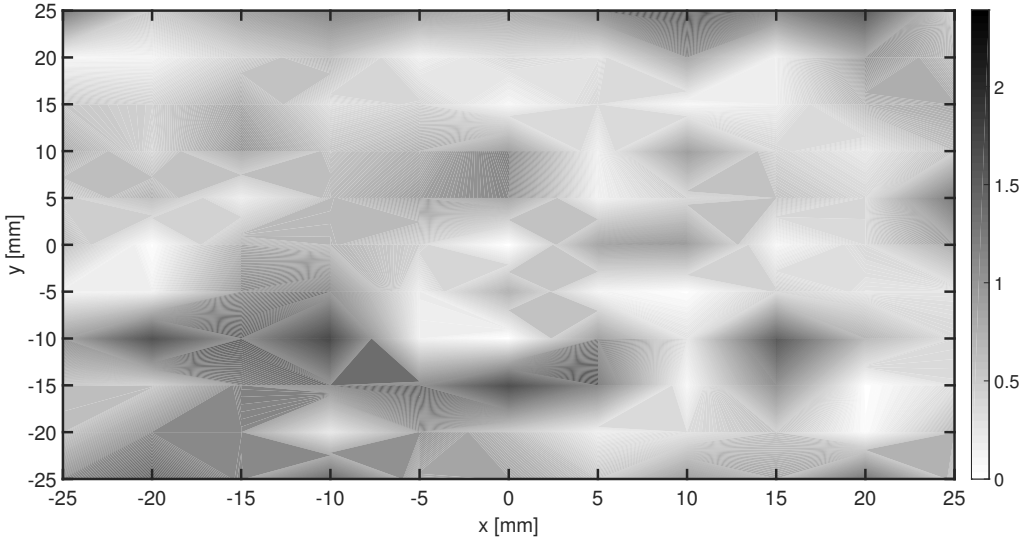


Figure 31: Expected signal at the diode output after 60 meters of clear silica fiber.

The homogeneity of the new detector geometry has been also checked for a beam energy equal to 1000 MeV.

As shown in Fig. 31, the error is less than 2.5 % over the range considered in the simulations, note that due to the small amount of primaries, the statistical error is approximately 1.5 %. The new geometry shows a similar behavior as the LSO based geometry, the influence of the geometry on the beam profile reconstruction should be negligible.

# 6 Proposal for a scintillator prototype

Some assumptions taken during the study shall be confirmed, as mentioned in this note the optical interfaces are almost perfect and the light trapping efficiency in the silica fiber to be evaluated. Prototypes might be down in order to asses this issues, in an ideal scenario, a beam test of few variants of the detector assembly shall be performed, the goal will be to calibrate the MC simulations. In particular few reflective materials can be tested as well as different options for the optical coupling of the various part of the detector assembly.

## 6.1 Material choice for early prototype

LSO crystal might be expensive for a early prototype phase, we proposed to used Saint Gobain BC-408 plastic scintillator as material for the prototype. As shown in Fig. 32, the light emission spectrum of this scintillator is similar to the LSO crystal, in particular the peak emission and matched almost perfectly the BCF-91a absorption spectrum.

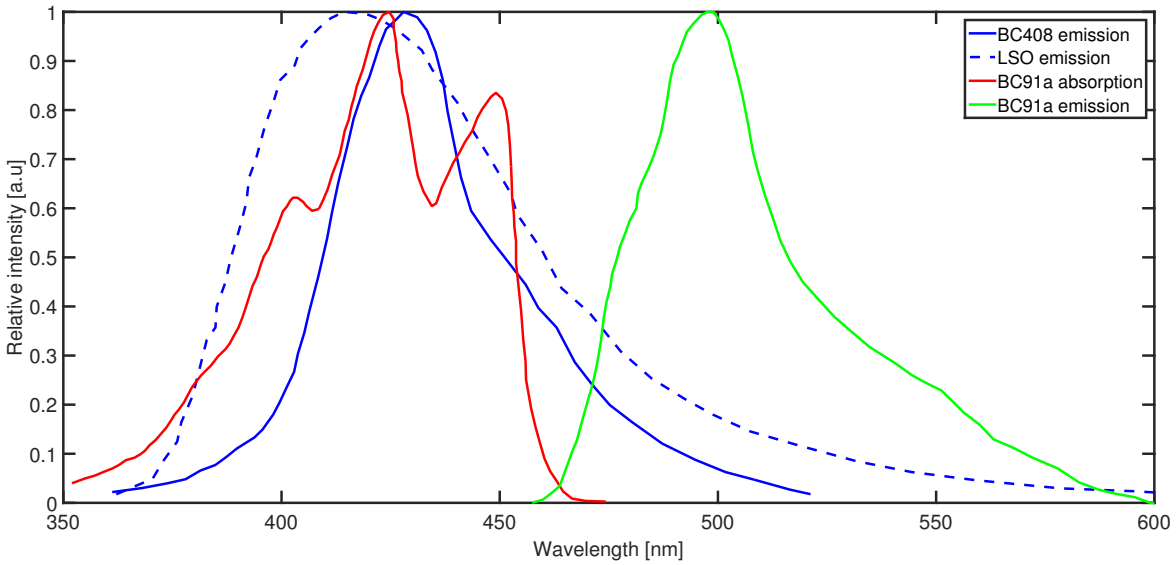


Figure 32: Optical spectrum of the Saint Gobain BCF-91A wavelength shifter and BC-408 scintillator.

The major difference of this material compared to the baseline design are is lower refractive index of the material ($n = 1.58$), lower light output ($\approx 11\ \gamma\ .\text{keV}^{-1}$) and lower density ($\rho = 1.032\ g.cm^{-3}$). With these parameters, the number of scintillation photons generated per proportion crossing the wire will be one order of magnitude lower, while the light collection will increase by almost 40 % due to the lower refractive index (see

Fig. 33). Nevertheless, most of the simulations uncertainties can be resolve with this cheaper material.

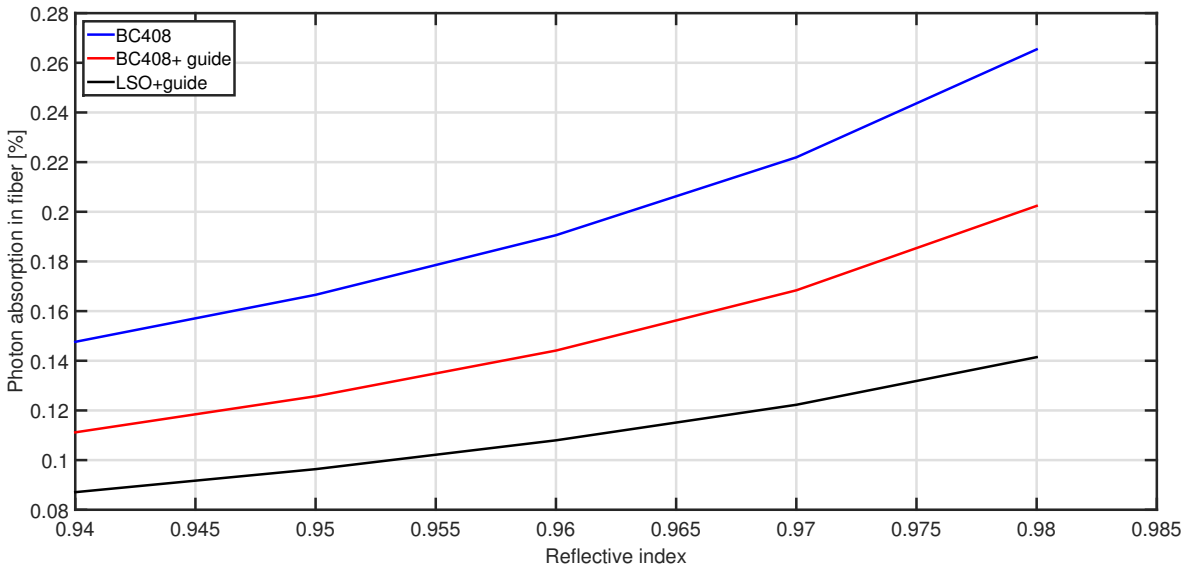


Figure 33: Estimation of the proportion of the scintillation photons absorbed in one WLS fiber different scintillator material and detector geometry

As shown in Fig. 33, the effect of a light guide can not be neglected, moreover in the MC simulations the optical boundaries are perfect, and small surface defect might have big impact on the light collection efficiency. Compare to a inorganic scintillator, the BC-408 is easy to machine, and the groove for the WLS fibers can be directly make in the scintillator. Nevertheless, it will be very useful to test the effect of the light guide on the performance of the detector.

For the detector, we are considering to use an acrylic plastic from Saint-Gobain (BC-800). This material has a density equal to $\rho = 1.19\ g.cm^{-3}$ and a refractive index equal to $n = 1.49$.

As mentioned, 2 types of WLS fibers can be used for our application, the BCF-91a from Saint-Gobain and the Y-11 from Kuraray. For the early prototype phase, a single manufacturer can be chosen, the fiber must have these specifications:

- A diameter equal to 1 mm
- Single cladding ($NA \approx\ 0.55$)

All the optical component shall glue together to improve the light transmission, the Saint Gobain BC600 (n=1.56) has been used for the simulation and might be the best candidate for the prototype.

A clear silica fiber with the same diameter as the WLS fiber must be chosen for the prototype phase. Molex is providing fiber in this diameter with an improved numerical aperture (0.48), manufacturer reference is JTFLH100010351400. Alternative fibers can be chosen, if the diameter and numerical aperture are similar as the ones of the WLS fiber. Pure silica fiber might be as well tested.

The reflectivity of the surrounding material is also important for the light collection, as shown in Tab 1, some materials with reflectivity above 0.95 are commercially available. Form the literature, Tyvek paper or Teflon seems to be the best candidate for scintillator application, thus at least one of this material shall be tested during the prototype phase.

| Reflector | Reflection coefficient |
|---|---|
| Teflon-3 layers | 0.992 |
| Teflon-4 layers | 1.000 |
| Glossy | 0.934 |
| VM2000 | 0.944 |
| VM2002 | 0.960 |
| VM3000 | 0.890 |
| Aluminum foil | 0.787 |
| Tyvek paper | 0.979 |
| Lumirror | 0.990 |
| Melinex | 0.969 |
| Titanium dioxide paint | 0.951 |

Table 1: Relative reflection coefficients, data from [7].

## 6.2 Light trapping in WLS and clear fiber

One of the first parameters to understand and test is the efficiency of the light transmission in the two types of fiber. A simple set up can be easily done to mesure the effect of the optical coupling between the 2 fibers, it is foreseen to use FC/APC fiber connectors for this. The test can be performed with the following procedure.

A short length of the WLS fiber ($l \approx 25\ cm$) can be mounted with a FC connector in one end. This setup can be installed in a box equipped with a blue LED, the light power at the exit of the connector will be measured. In as second step, a short silica fiber will be connected to the WLS fiber connector and the light power will be measured at the exit of the silica fiber with the same light power provided by the LED, thus it will be possible to characterize the efficiency of the transition between the fibers. In a second step, a longer silica fiber ($l \approx 10\ m$) can be used to measure the attenuation of the light in the clear fiber. It will be also interesting to spray a reflecting material on one of the side of the WLS fiber to measure the effect.

## 6.3 Early prototype

In a second step, a full detector assembly can be tested. Plastic scintillator are easier to machine and it will be possible to mount a LED on the scintillator itself. The set up will allow to test the efficiency of the optical coupling between the various elements of the detector and few reflective material. In particular it will be interesting to test:

- The coupling between the scintillator and the light guide with and without optical glue.

- The light power at the exit of the WLS fibers with the groove filled or unfilled with optical glue
- The effect of the various reflecting material on the light collection efficiency

For all these tests, it will be nice if the geometry of the detector is the same as the one simulates in the MC simulations:

- Scintillator size equal to $250 \times 45 \times 30$ $mm$.
- Light guide size equal to $250 \times 5 \times 30$ $mm$

The groove shall have a depth of at least 2 mm, a length of 250 mm and a wight of 1.5 mm (at least), the center of the groove shall be at 10 mm for the guide edges. The WLS fiber shall be long enough to fill the full groove length an allow enough space to mount the connector.

## 6.4 Final prototype

In a final stage, the best configuration found with the previous set up shall be tested in a real machine.Prior to the beam test, dedicated MC simulations shall be performed to estimate the expected light power, the goal of this test is to provide calibration factor to the MC simulations and to the data post processing. At this stage it will be nice to also test a prototype wilt the LSO crystal and test different WLS fibers.

# Part II
# Effect of beam losses on wire scanner scintillator readout, hypothesis and preliminary results

## 1 Hypothesis and input parameters

### 1.1 Hypothesis

In a first step, an too simplify the problem, we propose to study the effect of various beam losses scenario in a single elliptical period (one elliptical cryomodule followed by one LWU). It was assumed, that the contribution from upstream or downstream losses will be either too low to be detected or easily removed in the data analysis. For this case, no electromagnetic field was implemented in the simulation.

In a second step, the effect of beam loss has been simulated in 3 elliptical sections, the beam is transported in presence of magnetic field in the LWU.

A simplified geometry of an elliptical cryomodule has been implemented in the MC code (see Fig. 34), only the main components have been simulated, all the cryogenic pipe, cable, RF guide have not been implemented in the simulated geometry. Despite the fact that the Medium and High $\beta$ cavities are slightly different, the geometry is independent of the beam energy, a 5 cells cavity has been chosen for this study, which the one foreseen to be installed in the High $\beta$ section for beam energy above 570 MeV, the length of the cryomodule is about 6.5 meters. The quadruples consists in a single volume of copper.

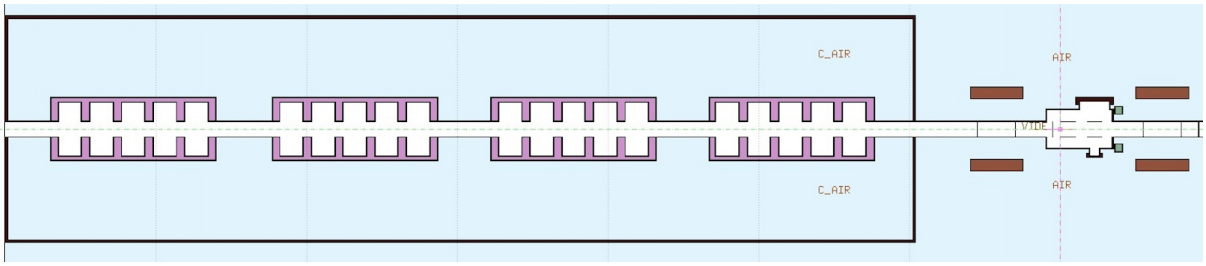


Figure 34: Geometry of the elliptical section implemented in the MC simulations.

The Linac Warm Unit (LWU) chamber has been simulated (see Fig. 3), the scintillator are attached to this chamber, the detector assembly is shown in Fig. 4. The minimum aperture in the LWU is 100 mm.

The scintillator material in these simulations are not the one foreseen to be used for the ESS WS system, in preliminary design phase of the WS detector BGO crystal was the primary candidate for the scintillator and all the simulations presented in this paper have been performed with this type of scintillator. nevertheless, since the geometry is identical, the signal to noise ratio shall be comparable for both versions of the detector.

For this simulations and in a first approximation, the beam sizes of the core were assumed to be constant in the cold linac with $\sigma_x = \sigma_y = 2$ mm. The beam has no energy

spread.

## 1.2 Beam distributions for the simulations

### 1.2.1 Full beam loss

In order to get a overall vision of beam loss effect on scintillators, a series of simulations have been performed with a pencil beam interacting with the beam pipe in the middles of quadrupoles. Simulations have been performed at 2 positions, in the middle of the upstream quadrupole and in the middle of the downstream quadrupole with respect of the detector position (see Fig. 3). The angle of impact was varying from 1 to 250 mrad and the beam energy from 200 to 2000 MeV.

A second series of simulations were done in order to check the effect of unwanted steering of the beam. The beams were created at the beginning of the cell in the center of beam pipe, an angular kick of 6 mrad and 10 mrad was given to the particles in order to have the interaction point of the beam center with the beam pipe in the center of the quadrupole and in the center of the cryomodule. the beam energy was varying from 200 to 2000 MeV. For this cases, only the beam core has been simulated and no electromagnetic field has been implemented.

For all the losses simulated, the beam impacts on the upper quadrant of the beam pipe.

### 1.2.2 Halo

During the operation of the WS system, the background noise will be mainly generated by losses due to particles lost from the beam halo (only the transverse halo has been considered in this study). In order to decrease the time of the MC simulations and have a good statistic, hollow beams have been simulated with a minimum radius of 10 mm. The origin of the beam is set at 100 mm upstream to the cryomodule entrance and transported in a single cell, without electromagnetic field.

The beam halo distributions are difficult to predict, several distributions have been considered in order to explore a large range of possibilities from a fully unmatched beam to almost perfect matching of the beam to the lattice. The distributions are identical in both planes.

In the worst case scenario, the particles will fill all the geometrical acceptance the cold linac, in a first approximation, the influence of the beam energy on the particle distribution in the phase space has been neglected. In real space, the particles have been generated in ring with a minimum radius of 10 mm and a maximum radius of 45 mm with a uniform density , the particles divergence was set to $\pm$ 7.5 mrad and to $\sigma_{x'}$=6 mrad, these values corresponds approximately to the geometrical acceptance of an elliptical section period, beam energy was scan form 200 MeV to 2000 MeV.

Similar simulations have been performed with different cut in the real space (15 $\sigma$ and 10 $\sigma$ of the beam core), with a distribution of the particle divergence equal to $\pm$ 6 mrad and $\pm$ 4mrad, all distributions have been considered uniform.

Based on the work presented in [8], several beam distributions were generated to simulate intermediate cases between a "fully filamented" beam and an ideal beam "matched" to the structure. Beam sizes were assumed to be independent of the beam energy, as well

as the distribution of the halo in the real space, while, in order to simulate the effect of the acceleration, the divergence of the particles is decreasing with the beam energy. Uniform and gaussian distributions have been simulated, for gaussian distribution it was assumed that the halo has an rms of 4 times the rms of the beam core (i.e 8 mm). Several cute has been simulated (20 $\sigma$,15 $\sigma$ and 10 $\sigma$ of the beam core), and i In the simulations. The beam halo divergence is increased by at least a factor 2 compare to the ideal beam in case of a gaussian distribution, for the flat distribution, the maximum divergence is $\approx$ 6 times the rms value of the ideal beam divergence. In addition, a smaller divergence has been simulated with an increase of few tens of percent compare to the distributions presented in [8], to simulate an optimal case with reduces losses. The evolutions of the divergence as function of the beam energy is shown in Fig. 35.

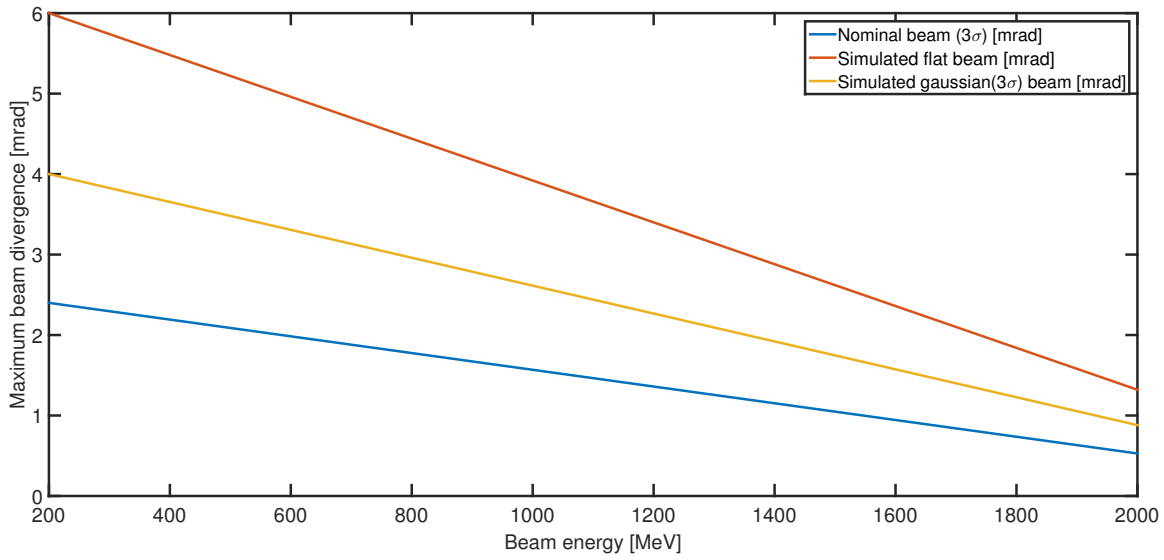


Figure 35: Maximum simulated divergence as function of the beam energy. In the document, the red curve is refereed to "flat", the yellow curve to "gauss high" and the blue one to "gauss low".

The parameters of the various simulated distribution are summarized in Tab. 2 and Tab. 3, in the next sections of this note, the distribution will be referenced by the name presented in the table.

Example of particle distributions are presented in annex.

## 1.3 Beam halo and effect of the quadrupolar field

Quadrupolar field might have an impact on the loss pattern and on the intensity of these losses. A basic set up has been implemented in the MC simulations to get a qualitative answer to this issue, for this study, 3 elliptical sections have been simulated, with all the LWUs equipped with scintillators.

The magnetic field was analytically generated in the beam pipe aperture with a gradient and effective length identical to the one foreseen for the operation at a given beam energy. Not that the field has no imperfection and no fringe field. In a first approximation, in particular at low energy, we considered that the charged particles interacting

| | Extension | |
|---|---|---|
| Name | real space | divergence |
| "fil. uniform" | $22.5\sigma$ uniform | $\pm$ 7.5 mrad uniform |
| "fil. gauss" | $22.5\sigma$ uniform | $\sigma_{x'}$ (1 rms) = 6 mrad |
| "15 6" | $15\sigma$ uniform | $\pm$ 6 mrad uniform |
| "15 4" | $15\sigma$ uniform | $\pm$ 4mrad uniform |
| "10 6" | $10\sigma$ uniform | $\pm$ 6 mrad uniform |
| "10 4" | $10\sigma$ uniform | $\pm$ 4mrad uniform |

Table 2: Summary of the beam distribution simulated when they are independent of the beam energy. Extension in real space are given in term of $\sigma$ of the beam core

| | Extension | |
|---|---|---|
| Name | real space | divergence |
| "20sig." | $20\sigma$ uniform | flat |
| "15sig. flat" | $15\sigma$ uniform | flat |
| "15sig. gauss" | $15\sigma$ gauss | gauss high |
| "10sig. flat" | $10\sigma$ uniform | flat |
| "10sig. gauss" | $10\sigma$ gauss | gauss high |
| "Nominal" | $10\sigma$ flat | gauss low |

Table 3: Summary of the beam distribution simulated, extension in real space are given in term of $\sigma$ of the beam core type, the divergence can be seen in Fig. 35.

with the quadrupole yoke are stopped in the material, his the magnetic field on the iron magnet can be neglected.

A single beam energy has been simulated (400 MeV) and only the 5 last beam of Tab. 3 have been used as particle source. The particles were transported with and without the magnetic field activated, in both cases the energy deposited in each scintillator has been scored.

# 2 Preliminary results

## 2.1 Full beam loss

As shown in Fig. 36 to Fig. 38, the energy deposited in the detector 1 is strongly dependent of the losses angle, and less on the beam energy. Compare to the scintillator signal (less than 1 keV per primary), the beam loss signal on the detector will be much higher than the expected signal during a profile measurement.

From these results, it seems possible to detect the position of a losses, also detect the direction of the loss, a clear difference on the signal of each detector can be detected (see Fig. 38).

For the cases of unwanted beam steering, like the previous results, the WS acquisition will be fully saturated as shown in Fig. 39 and Fig .40.

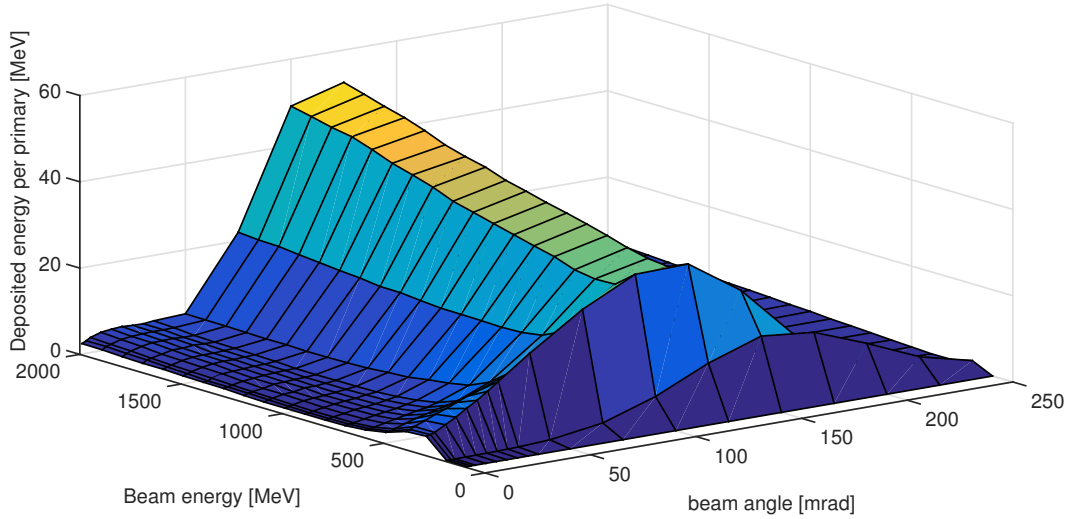


Figure 36: Estimated energy deposited in detector 1 as function of the beam energy and angle of impact. The loss is in middle of the upstream quadrupole.

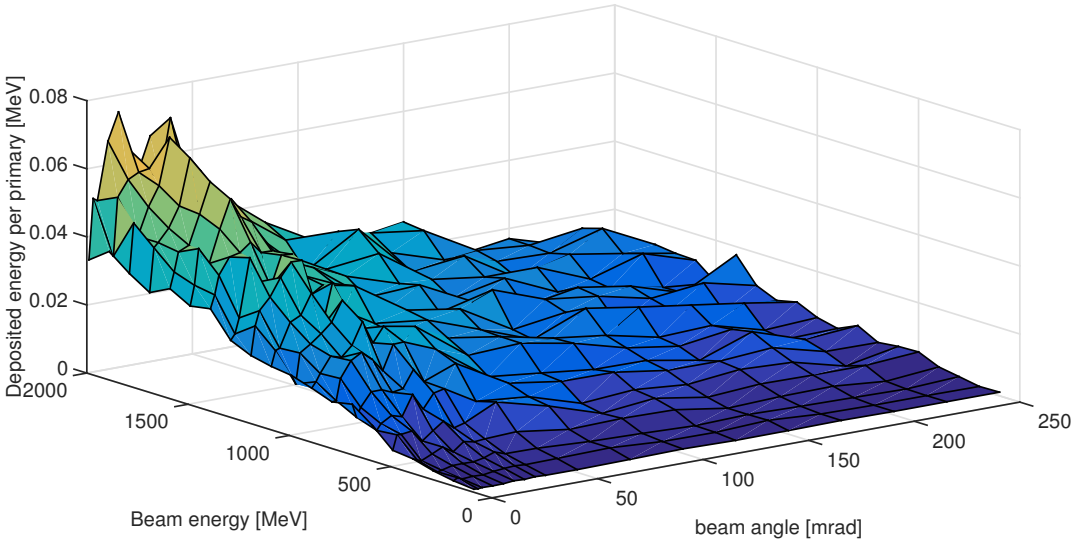


Figure 37: Estimated energy deposited in detector 1 as function of the beam energy and angle of impact. The loss is in middle of the downstream quadrupole.

For the 6 mrad case, it is interesting to note that the loss direction can be detected and the signal on the detector 1 increase rapidly below 400 MeV and slowly above and up to 2 GeV. This can be explain by the cinematic of the reaction ad the detector geometry, the signal on the scintillator is dominated by the energy deposition induced by protons. Below 400 MeV, more than 80 % of the signal is generated by protons, above this energy, the protons are emitted in a cone which becomes smaller when the beam energy increases, as consequence a smaller portion of this particle interacts with the scintillator and their contribution to the signal decreases. Nevertheless, the production of secondaries particles

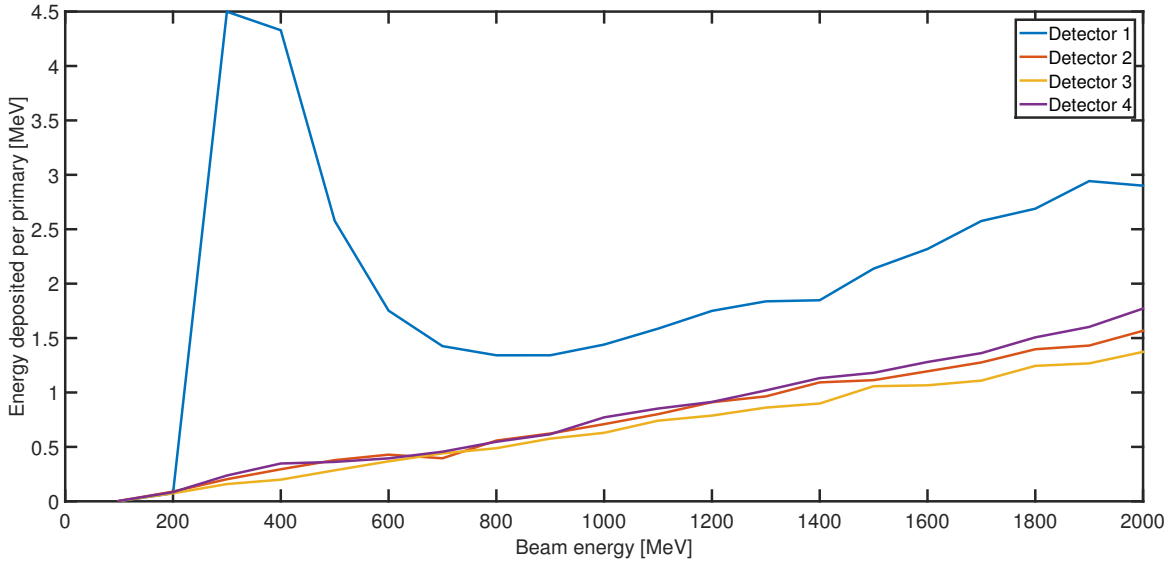


Figure 38: Evolution of the deposited energy as function of the beam energy on the 4 detectors, the beam impacts in the upstream quadrupole with an angle of 3 mrad.

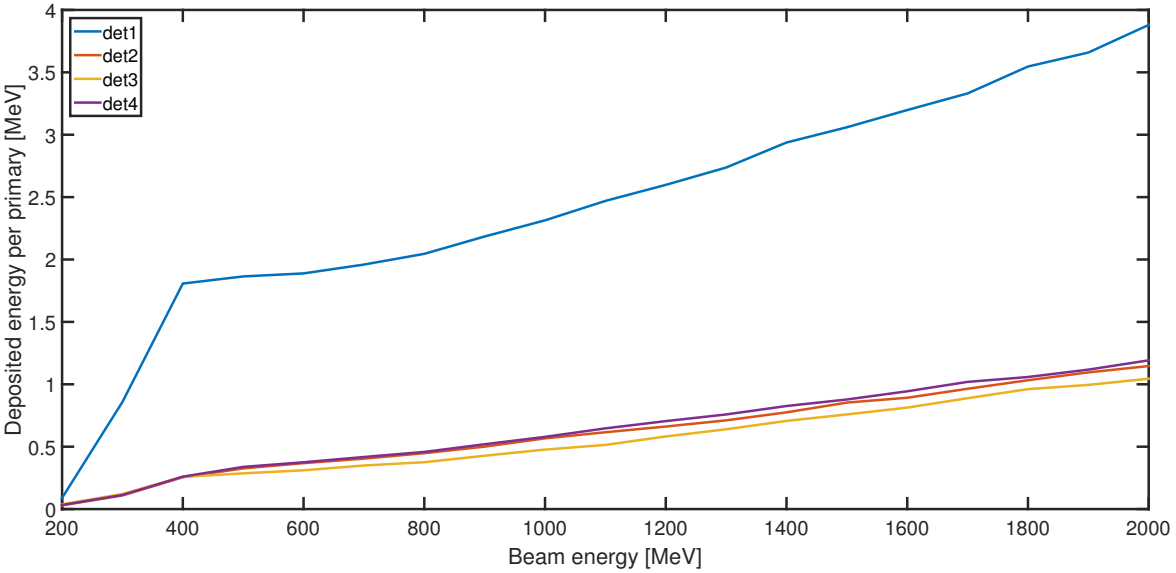


Figure 39: Evolution of the energy deposited in each scintillator as function of the beam energy, the impact is in the middle of the upstream quadrupole corresponding to an angular kick of 6 mrad.

increases with the energy and therefor increase the signal, at 2 GeV, 50 % of the signal is induced by the secondaries particles. Note the the signal on the other detectors increase almost linearly with the beam energy.

For a beam impacts in the middle of the cryomodule, at low energy the signal on all the detectors are more or less equal, the direction of the loss can be detected only at high energy. In this case, the beam and the product of the induced shower interact with more matter than in the previous case, due to this interaction, at low energy the flux of

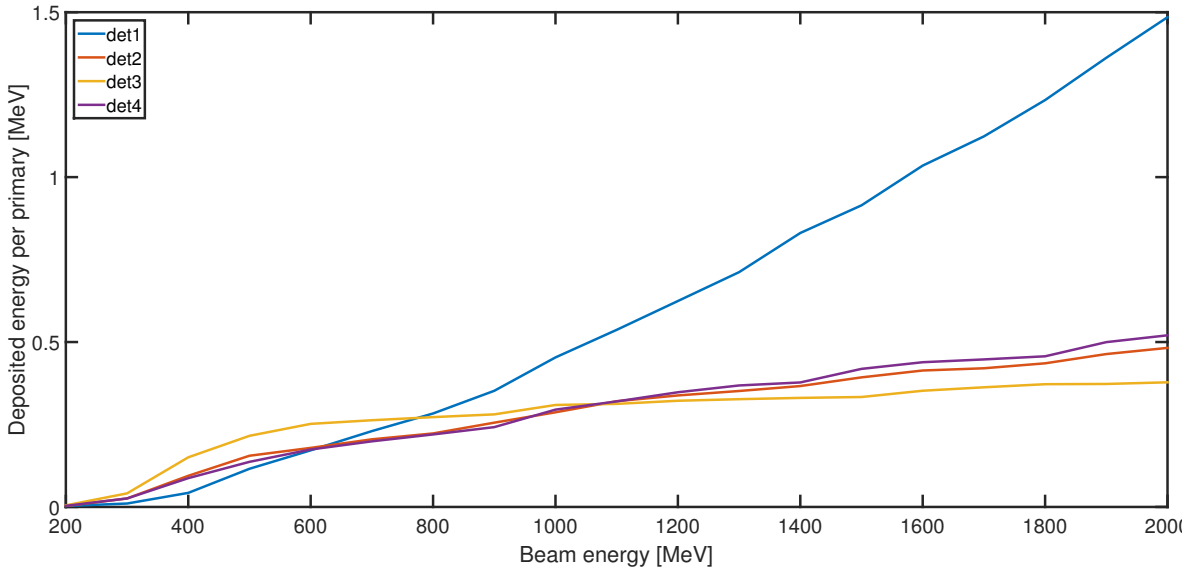


Figure 40: Evolution of the energy deposited in each scintillator as function of the beam energy, the impact is in the middle of the upstream cryomodule corresponding to an angular kick of 10 mrad.

particles will be almost uniform at the scintillator location, while as the energy increases, the beam interacts less an less with the matter leading to a rapid increase of signal of the detector positioned in the same quadrant of the loss.

## 2.2 Halo

For a given distribution and a given beam energy, as shown in Fig. 41 the signal on the 4 detectors is almost identical, thus all the following results are presented for a single detector.

### 2.2.1 Energy deposition

With the same particle distribution for the energies considered, the energy deposited in the detector increases with the beam energy (see Fig. 42). it also appears clearly that the beam divergence has a strong impact on the losses, more important than the extension in the real space.

The same influence of the beam halo divergence can be seen when the influence of the acceleration has been simulated (see Fig. 43).

For all the beam distributions considered, the peak energy deposition is around 400 MeV. Above this energy, the signal is decreasing with the beam energy due to the smaller and smaller divergence. At the exception of the largest (i.e "20 sig.") beam the signal is almost zero above 1500 MeV, nevertheless it might be an artifact of the simulation due to the small statistic i and of the cut in the particle distribution, some losses should be expected in the high energy range of the ESS linac.

The losses might be an issue between 200 and 600 MeV, which corresponds to the ESS medium $\beta$ section energy range. The influence of the beam divergence is important,

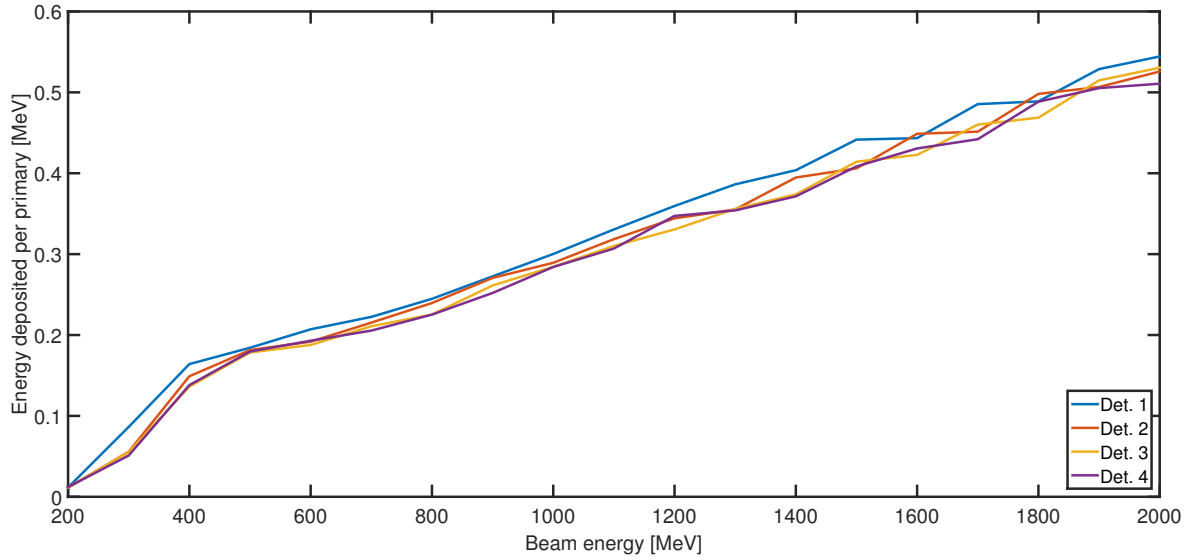


Figure 41: Evolution of the energy deposited in each scintillator as function of the beam energy, for the beam distribution "fil. uniform"

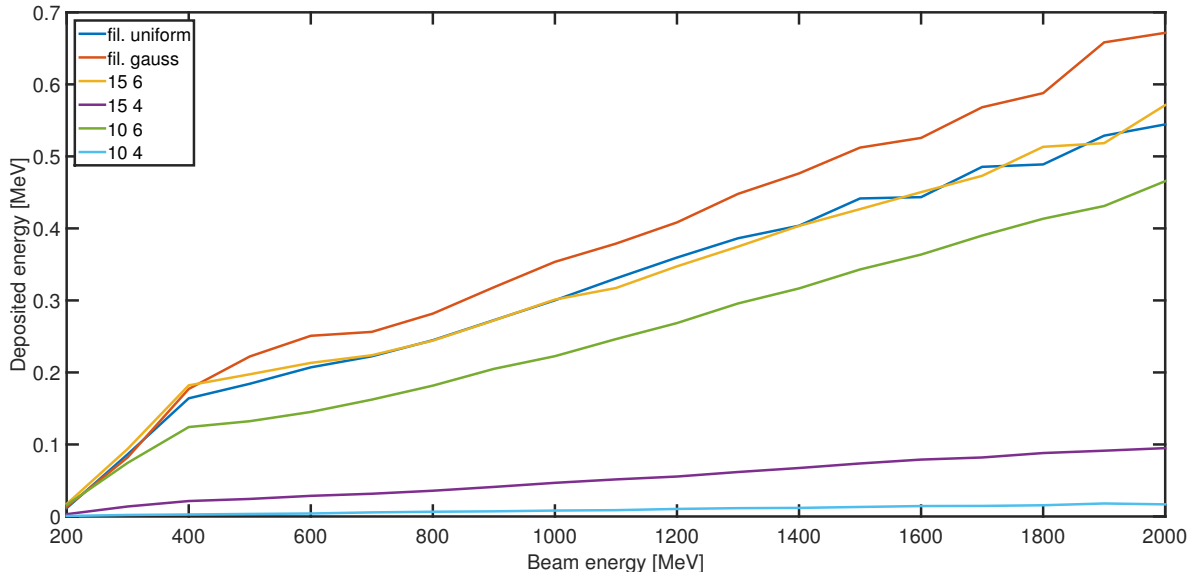


Figure 42: Evolution of the energy deposited in one scintillator as function of the beam energy, the distributions in this figure are independent of the beam energy.

with a lower divergence ("nominal" beam in Fig. 35) the energy deposited is almost null above 400 MeV.

Due to the simplified geometry and the low statistic present in the simulation, the peak at 400 MeV might be artifact of the MC simulations, depending on the amount of matter that the loss particles will see this peak might slightly move. These data are certainly not a representative of the losses expected in the ESS linac, nevertheless, they can be used to set the operating domain of the WS.

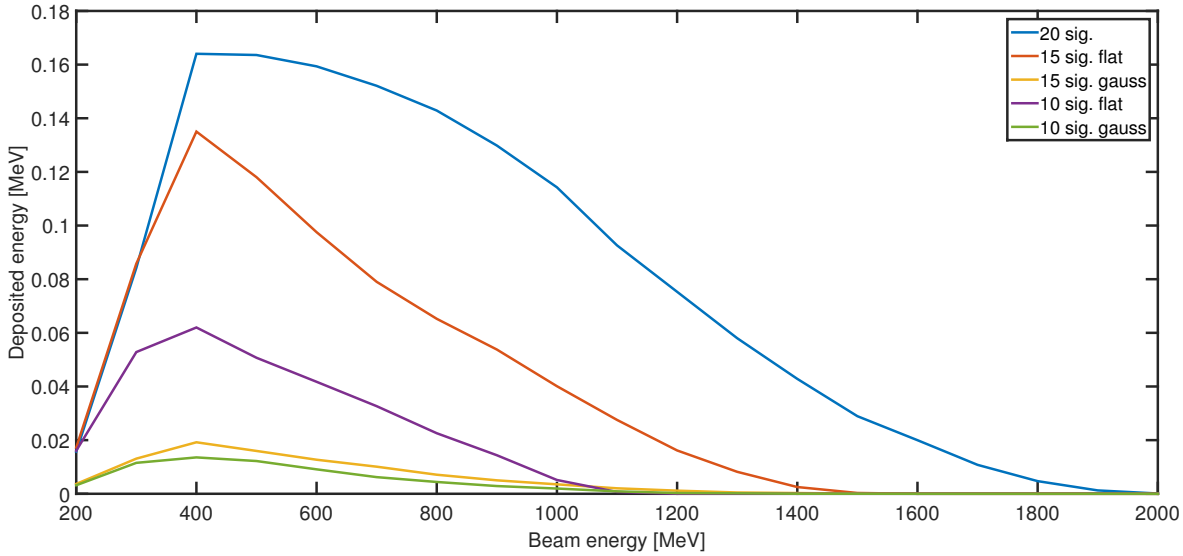


Figure 43: Evolution of the energy deposited in one scintillator as function of the beam energy, beam halo divergence is decreasing with the energy .

### 2.2.2 signal

The previous results were uses to estimate the Signal to Noise Ration (SNR) expected during a beam profile measurement. The expected peak signal from the WS as been simulated with the same geometry and assuming a 40 $\mu m$ tungsten wire. The minimum signal is expected for a beam energy of 400 MeV, the maximum signal at 2000 MEV. In post processing and with the date presented in the previous section, the background signal has been estimated for various proportion of particles in the halo and the expected Signal to Noise Ration (SNR) during a beam profile measurement has been calculated for the lowest expected signal (400 MeV). The results are summarized in Fig. 44 and Fig. 45. Note that only the effect of beam losses has been estimated, other factor may degrade the SNR (electronic noise, interference....).

In all cases, if the $10^{-9}$ of the particles are in the halo as simulated in the MC code, the SNR is better than $10^4$, if this proportion increase to $10^{-6}$ the SNR will be $\approx$ 100 in the worst case and up to $10^{-5}$ in the best case simulated. At High energy, for the cases with a divergence decreasing with the beam energy, the SNR increases. The reconstruction of the beam profile might be compromised if the losses in the ESS superconducting linac is too high.

## 2.3 Effect of quadrupolar field

### 2.3.1 Energy deposition

As shown Fig. 46 to Fig. 48, a clear difference on the signal is induced by the magnetic field. For most of the cases considered, in absence of magnetic field, the maximum signal is observed in the second elliptical section and the signal on the 4 scintillators of each LWU is more or less equal. For the "nominal" beam, the peak is observed in the last LWU, in the first one, the signal is almost null ($\approx$10 eV per primary).

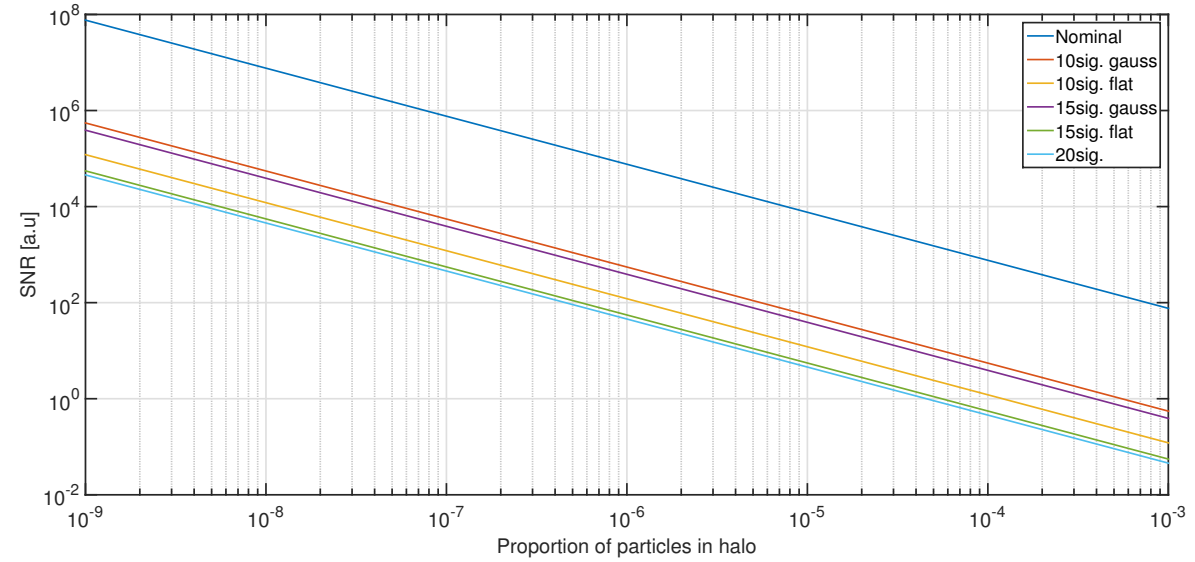


Figure 44: Expected SNR at 400 MeV for beam halo distribution dependent of the beam energy.

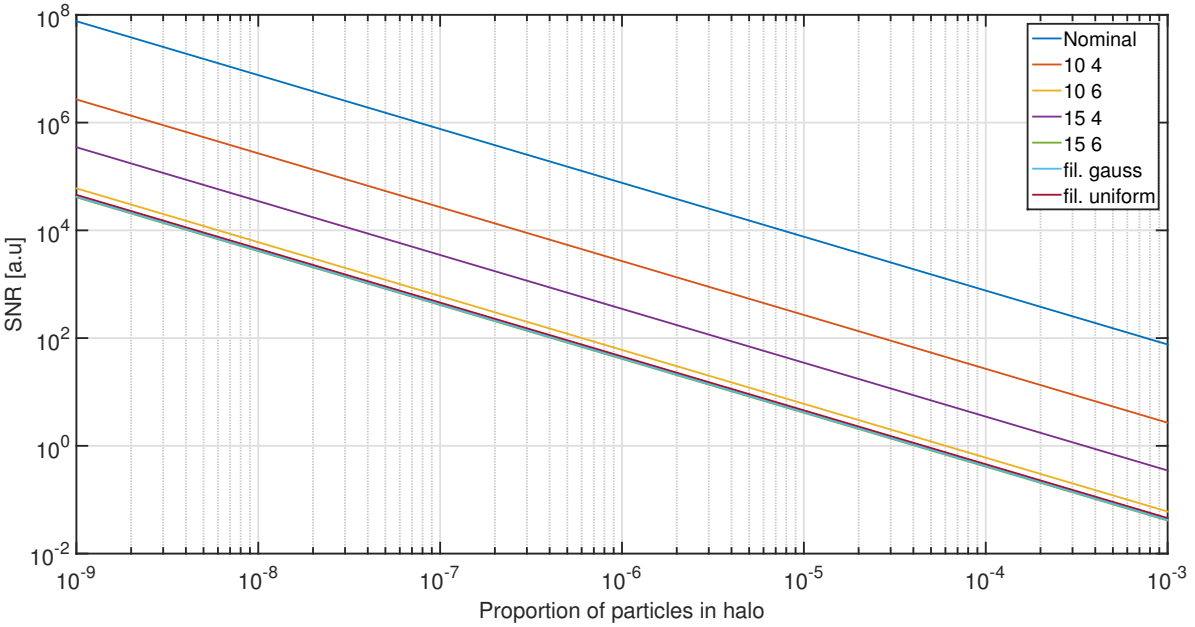


Figure 45: Expected SNR at 400 MeV for beam halo distribution independent of the beam energy.

When the magnetic field is activated, the peak signal appears in the first section, moreover, the signal is not identical on the 4 scintillators. It has to be noted that the first quadrupole of the LWU is focussing the beam in the horizontal plane and is positioned just upstream the scintillator assembly. Due to the detector assembly (see Fig. 4), the flux of particles is higher on the detector 1 ad detect 3, thus the signal is higher on the these scintillators.

For all the beams simulated, the energy deposited in the scintillator of the last LWU

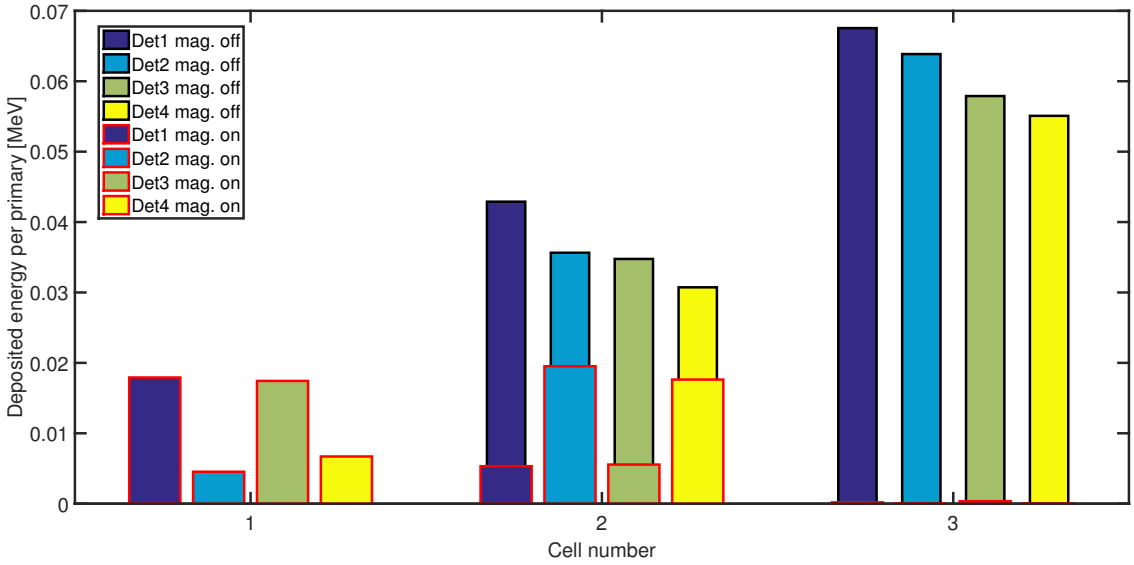


Figure 46: Energy deposited per scintillator for 3 consecutive elliptical sections, with magnetic field on or off. The particle source in the simulations is "nominal" (see Tab. 3 )

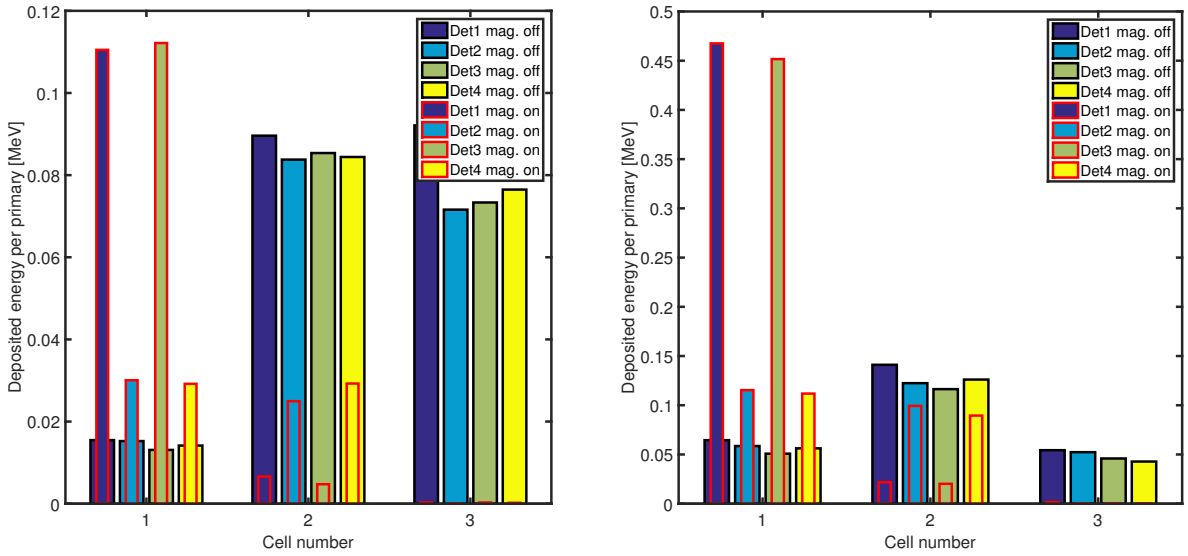


Figure 47: Energy deposited per scintillator for 3 consecutive elliptical sections, with magnetic field on or off. The particle sources in the simulations are "10 sig. gauss" for the left plot and "10 sig. gauss" for the left plot (see Tab. 3).

is reduced by few orders of magnitude if the magnetic filed is activated. The energy deposition for these cases are in the range for few eV to few hundred of eV. It is interesting to note that the transmission of the beam particle in the third elliptical section is almost 100 %, thus the signal is generated by beam losses in the first and the second section. From these results, and prior to further simulations, it can be concluded that the scintillator are almost insensitive to upstream beam losses.

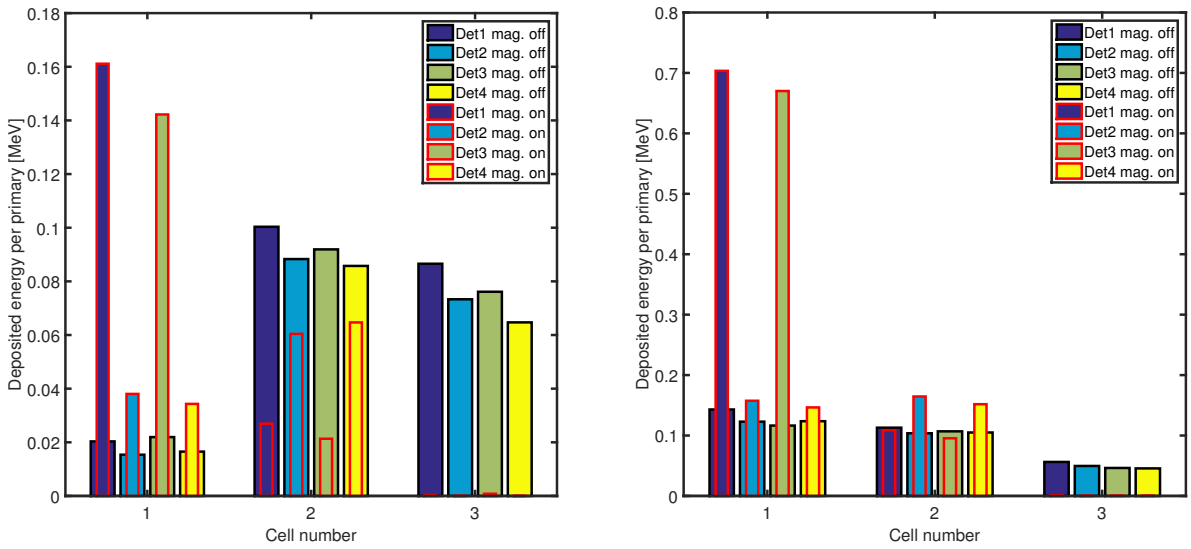


Figure 48: Energy deposited per scintillator for 3 consecutive elliptical sections, with magnetic field on or off. The particle sources in the simulations are "10 sig. gauss" for the left plot and "10 sig. gauss" for the left plot (see Tab. 3).

### 2.3.2 signal

The results presented in the previous section was used to estimate the expected SNR for the 3 LWUs, the results are show in Fig. 49 to Fig. 51.

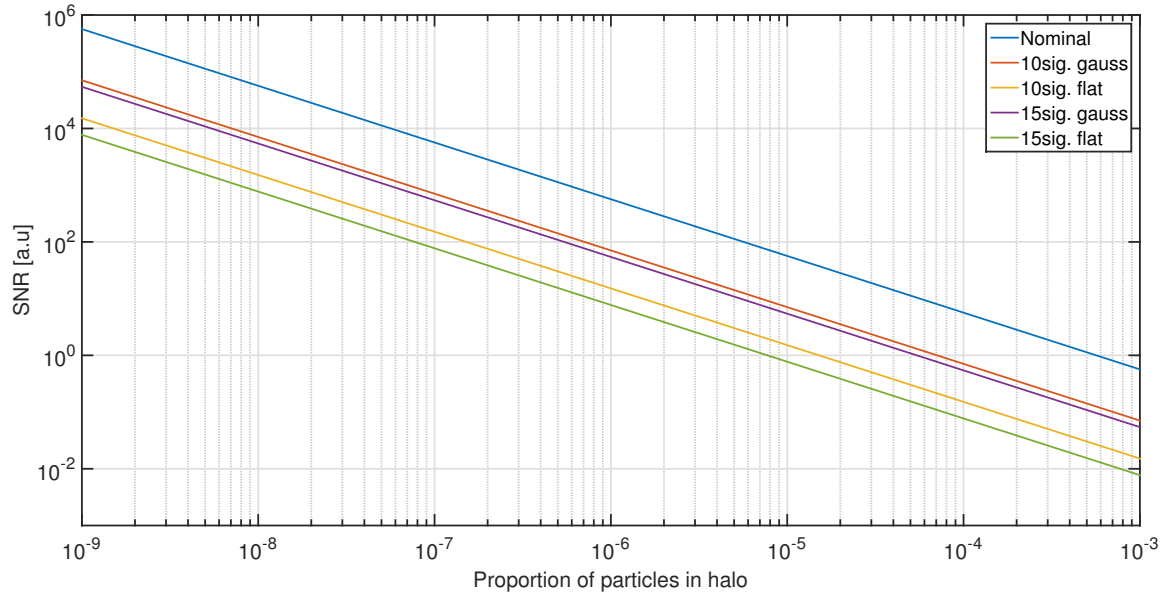


Figure 49: Expected SNR at 400 MeV in the first simulated LWU with magnetic field activated.

In the first LWU, the SNR is decreases by almost a factor 200 for the "nominal" beam and almost a factor 10 for the other simulated beams compare to the one estimated in

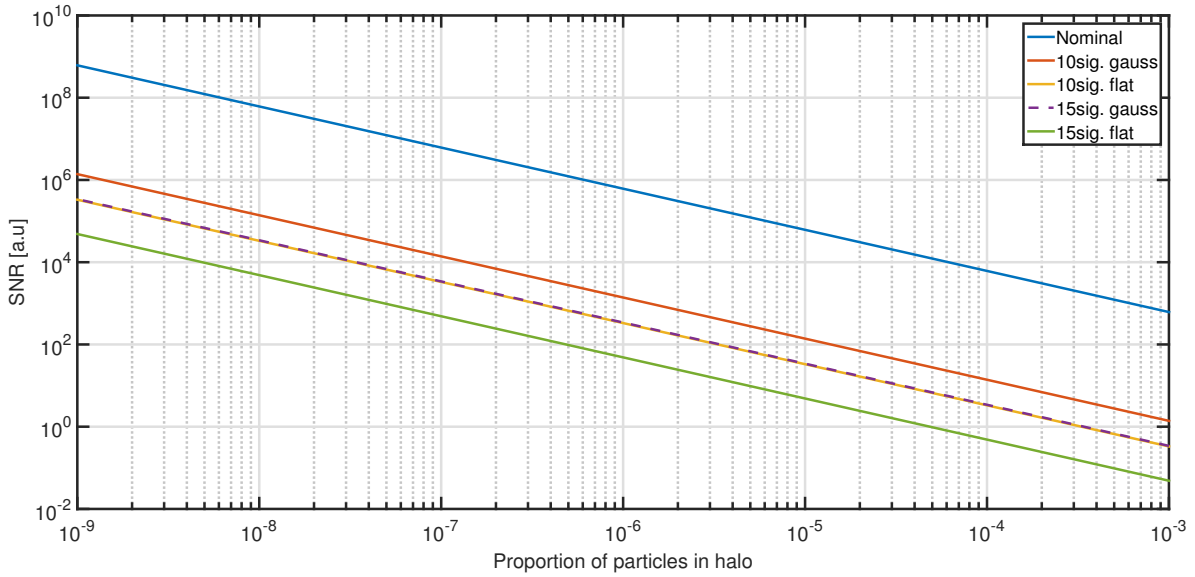


Figure 50: Expected SNR at 400 MeV in the second simulated LWU with magnetic field activated.

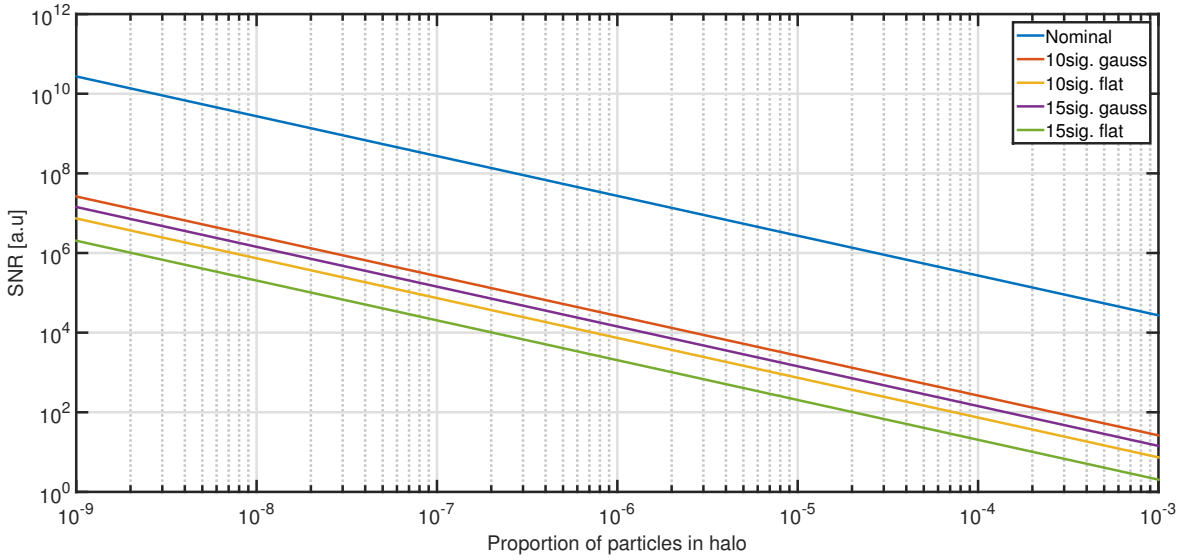


Figure 51: Expected SNR at 400 MeV in the third simulated LWU with magnetic field activated.

absence of magnetic field and a single LWU (Fig. 45). In the second LWU, the SNR is almost identical, while in the third LWU, the SNR is improve by a factor up to 100.

From the results presented in the section, it could be concluded that the lattice simulated in the MC code, can be seen as a filter. After few sections, it seems that the beam particles outside the transverse acceptance are lost, and the transmission is almost 100 %. As mentioned previously, this series of simulations must be considered as an indication of the global response of the scintillator to the beam losses. The input beams, the geometry and the magnetic field are simplified and no error has been considered like the

misalignment of the magnet. Also, in the MC simulations, the cryomodule is considered as a drift in the point of view of the beam dynamics, this case corresponds to a detuned cavities not feed with RF pows, this case might not be so realistic, it expected that the field of the cavities will have also an influence on the beam loss pattern.

# Part III
# Conclusion and Outlook

## Detector concept

The detector concept proposed in this note seems interesting for the ESS application, in particular the absence of sensitive electronic in the tunnel area. The signal is expected to be less perturb by the interference of a high power accelerator environment (in particular the RF system), the conversion from light to current in the electronic cabinet will allow a cleaner signal.

Nevertheless, some assumptions taken during the study shall be confirmed, as mentioned in this paper the optical interfaces are almost perfect and the light trapping efficiency in the silica fiber to be evaluated, for this it is excepted to develop a small set-up in our laboratory.

Prototypes might be down in order to asses this issues, in an ideal scenario, a beam test of few variants of the detector assembly shall be tested with beam, the goal will be to calibrate the MC simulations. In particular few reflective materials can be tested as well as different options for the optical coupling of the various part of the detector assembly. This phase will allow also to finalize the choice of the WLS fiber.

## Effect of beam losses

The studies presented in this note might be far from what will be observed in the ESS linac, the low statistic in the MC simulations as well as the arbitrary beam distributions induced certainly large uncertainty on the results. Nevertheless, the cases presented in this note are setting the limits for the expected beam losses.

These preliminary studies show that the WS detectors are quite sensitive to beam losses, the performance of the WS might suffer if the losses exceed $10^{-6}$ and if the halo is not mitigate.The detector concept proposed for the ESS wire scanner shows an interesting sensitivity to the beam halo parameters. In high power hadron linac, matching the halo seems a better alternative to the classical core matching in order to reduce the beam losses toe an acceptable level [9], the detector part of the WS system might be used not only to measure the beam core profile but also, together with other monitors like the Beam Loss Monitor[10], to match the beam halo.

In order to confirm the ability of the WS system to be used for the halo matching, the particles distributions used for the simulation must be refined with dedicated beam dynamic simulations.

# References


[1] M. Eshraqi et al., "the ESS linac", in *Proc. IPAC14*, Dresden, Germany, THPME043,

[2] B. Cheymol, "ESS wire scanner conceptual design" ESS Technical note ESS-0020237

[3] S. Filippov et al."Experimental Performance of SPD/PS Detector Prototypes" CERN-LHCb-2000-031

[4] L. Zhang et al. "LSO/LYSO Crystals for Calorimeters in Future HEP Experiments" in *J. Phys.: Conf. Ser. 293 012004* 2011

[5] A. Ferrari, P.R. Sala, A. Fasso, and J. Ranft, "FLUKA: a multi-particle transport code" CERN-2005-10 (2005), INFN/TC_05/11, SLAC-R-773.

[6] F. Duru et al."CMS Hadronic EndCap Calorimeter Upgrade studies for SLHC Cherenkov light collection from quartz plate" CMS note 2007/019 May 2007

[7] M. Janecek and W. Moses, "Optical reflectance measurements for commonly used reflectors" http://escholarship.org/uc/item/82r9k9rn

[8] R. Miyamoto., "An ESS linac collimation study", in *Proc. HB14*, East-Lansing, MI, USA

[9] N. Chauvin et al.., "Halo Matching for High Intensity Linacs and Dedicated Diagnostics", in *Proc. HB14*, East-Lansing, MI, USA

[10] I. Dolenc Kittelmann, "Simulations and Detector Technologies for the Beam Loss Monitoring System at the ESS Linac;" in *Proc. HB16*, Malmo, Sweden

# List of Figures

# A Secondary particle flux

The spectra of secondaries particles reaching the detector surface for beam energies equal to 570, 1000, 1300 and 1500 MeV are shown in Fig. 52 to Fig. 59.

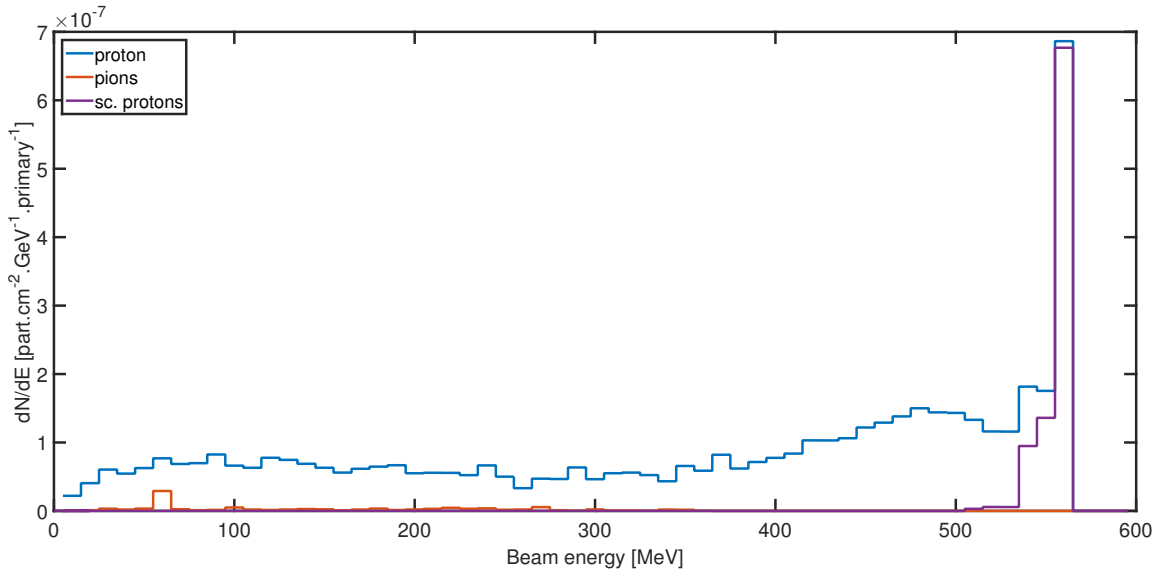


Figure 52: Protons and pions spectra on the detector surface for a beam energy equal to 570 MeV.

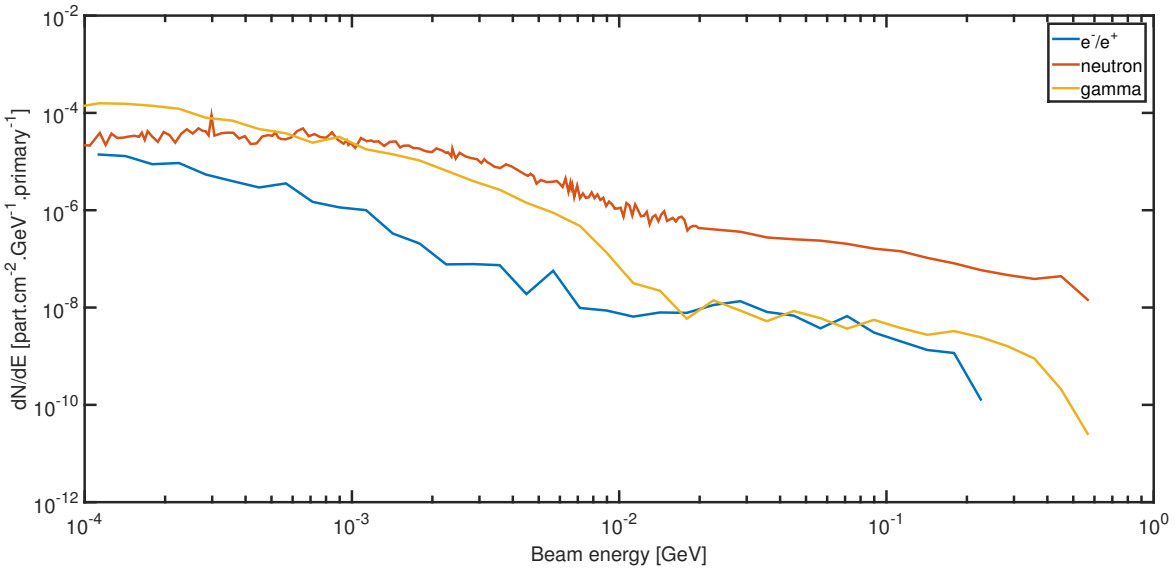


Figure 53: Neutron, gamma, election and positron spectra on the detector surface for a beam energy equal to 570 MeV.

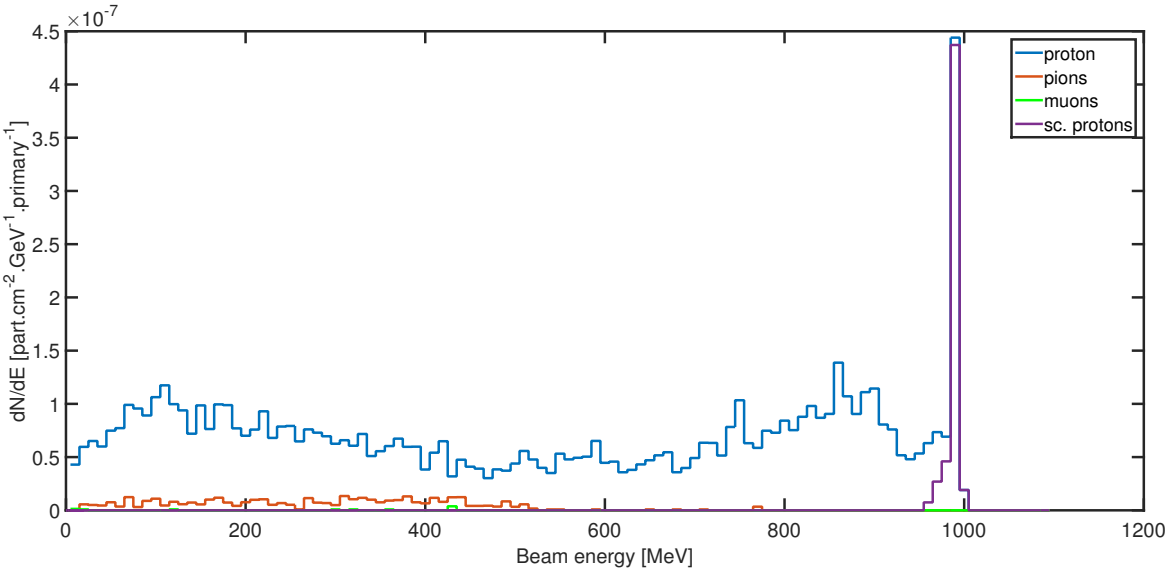


Figure 54: Protons and pions spectra on the detector surface for a beam energy equal to 1000 MeV.

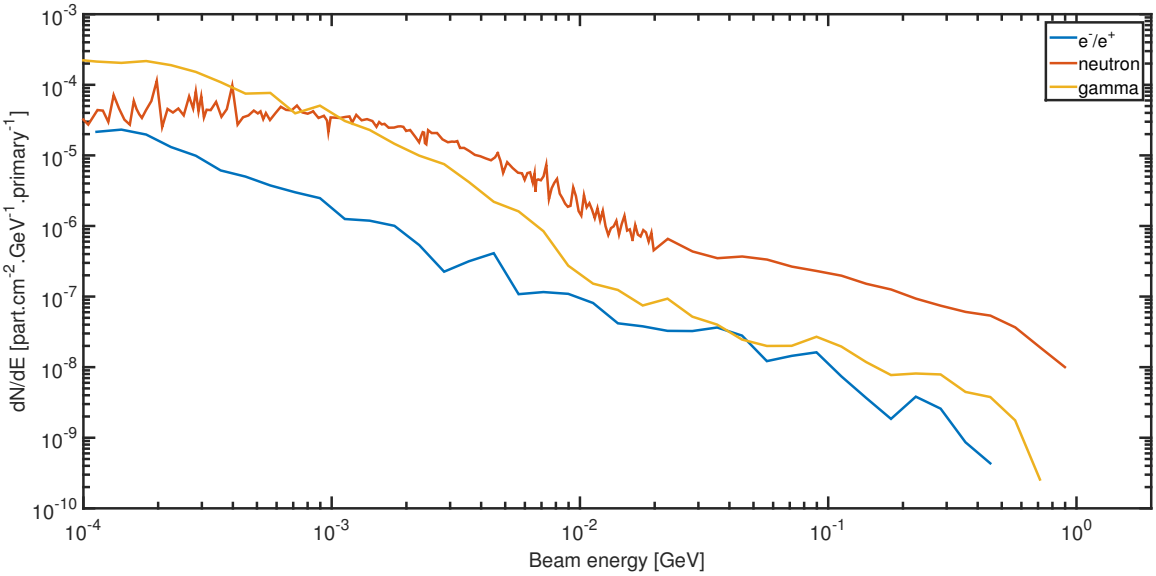


Figure 55: Neutron, gamma, election and positron spectra on the detector surface for a beam energy equal to 1000 MeV.

# B Detector homogeneity

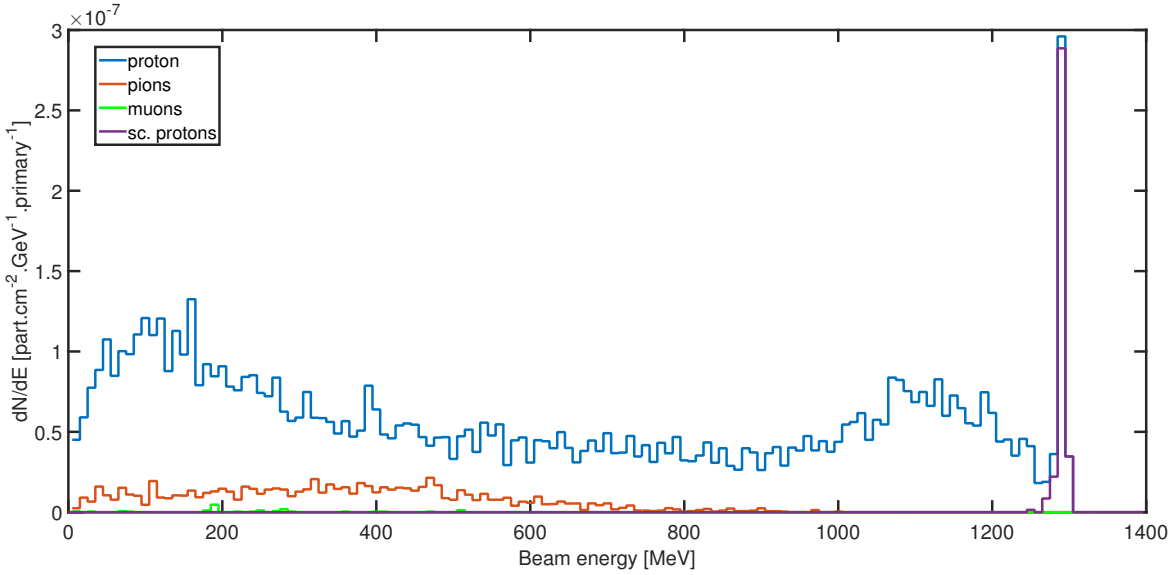


Figure 56: Protons and pions spectra on the detector surface for a beam energy equal to 1300 MeV.

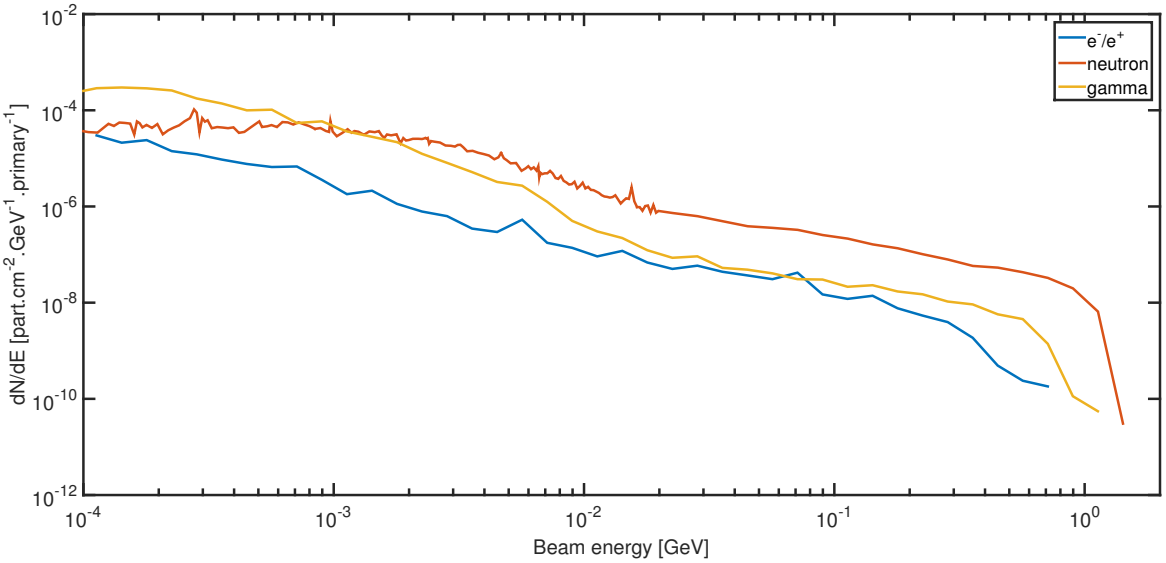


Figure 57: Neutron, gamma, election and positron spectra on the detector surface for a beam energy equal to 1300 MeV.

# C Particles distribution in transverse plane

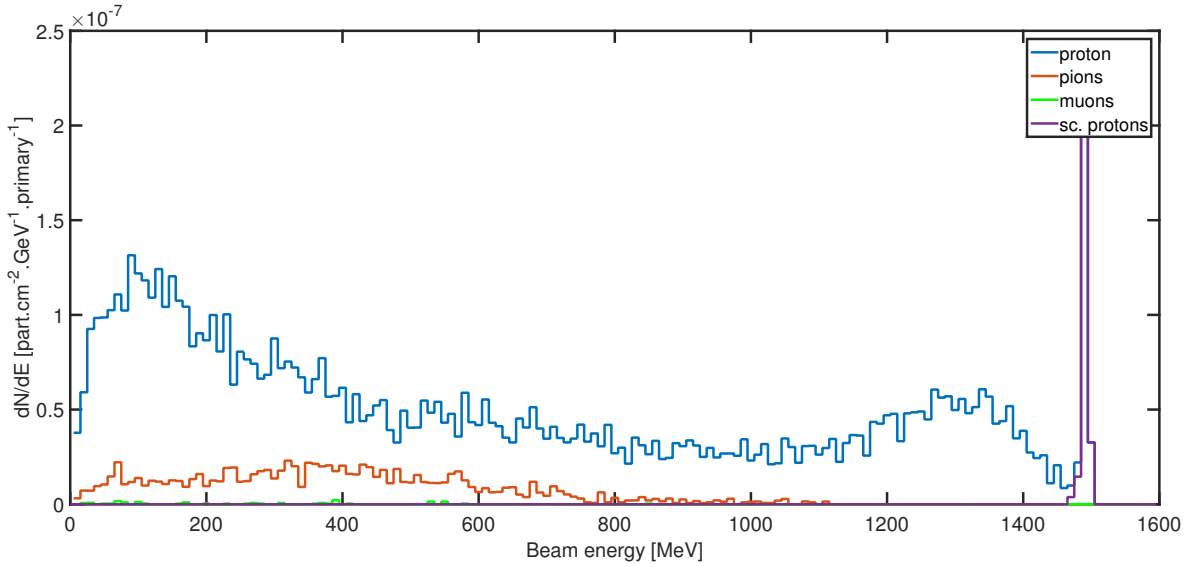


Figure 58: Protons and pions spectra on the detector surface for a beam energy equal to 1500 MeV.

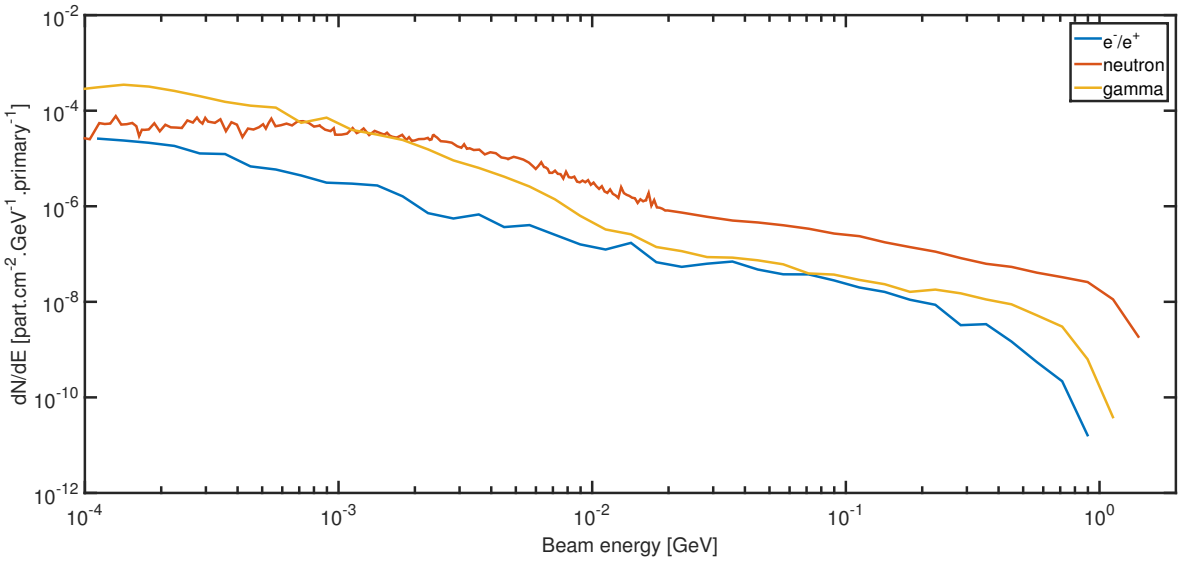


Figure 59: Neutron, gamma, election and positron spectra on the detector surface for a beam energy equal to 1500 MeV.

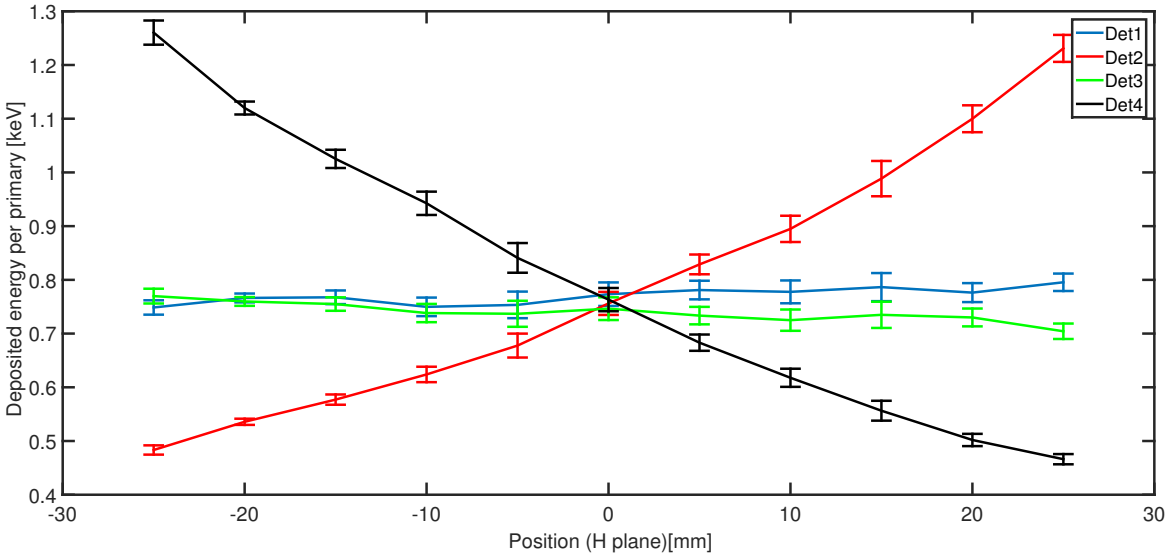


Figure 60: Energy deposited in each of the detectors at y=0 when the horizontal plane is scanned beam energy is 200 MeV. Similar results are observed in the vertical plane with an inversion of the detector curves (i.e the flat curves are obtained with detector 2 and 4)

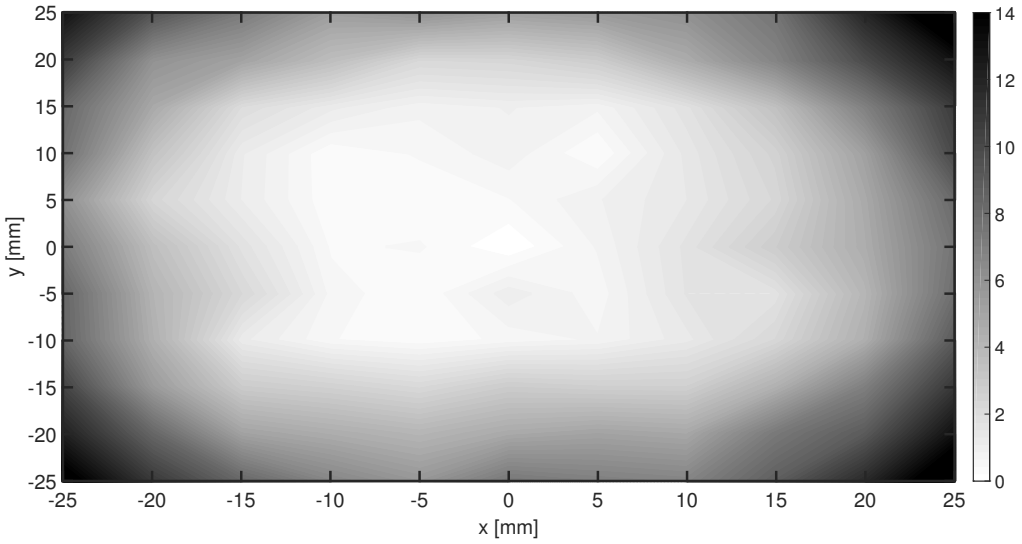


Figure 61: Absolute error map as function of the wire position, the beam energy is equal to 200 MeV.

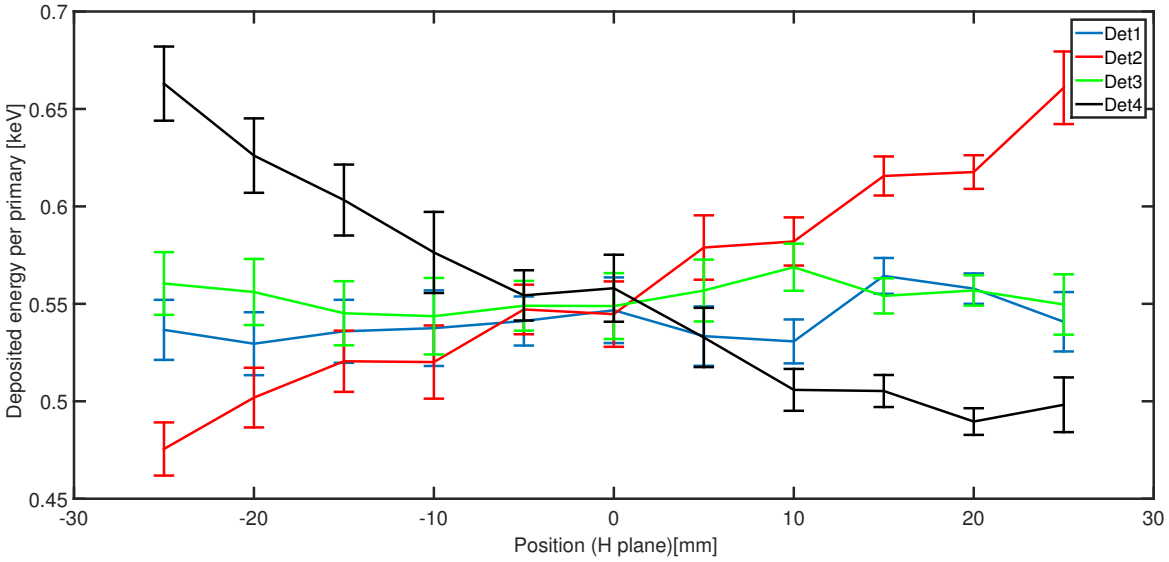


Figure 62: Energy deposited in each of the detectors at y=0 when the horizontal plane is scanned beam energy is 570 MeV. Similar results are observed in the vertical plane with an inversion of the detector curves (i.e the flat curves are obtained with detector 2 and 4)

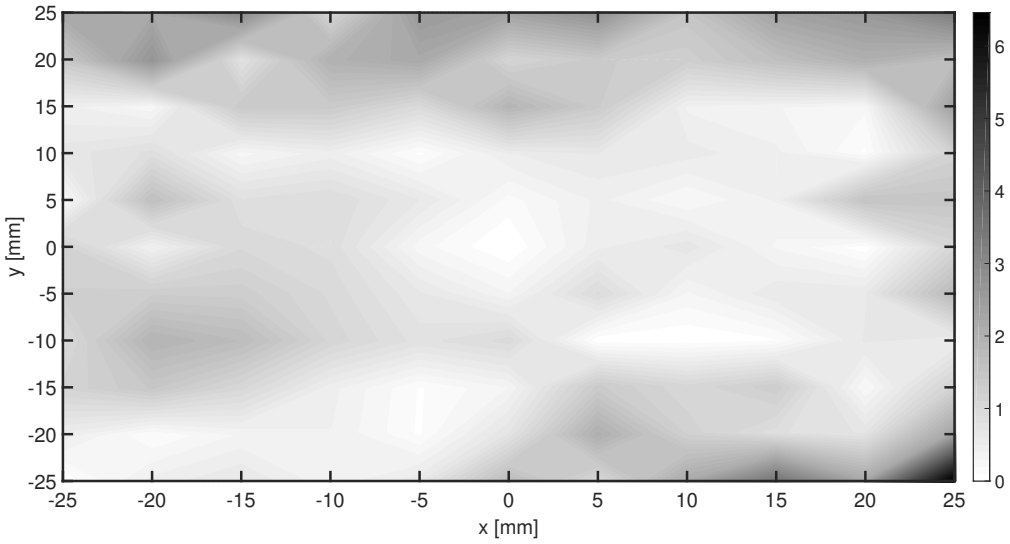


Figure 63: Absolute error map as function of the wire position, the beam energy is equal to 570 MeV.

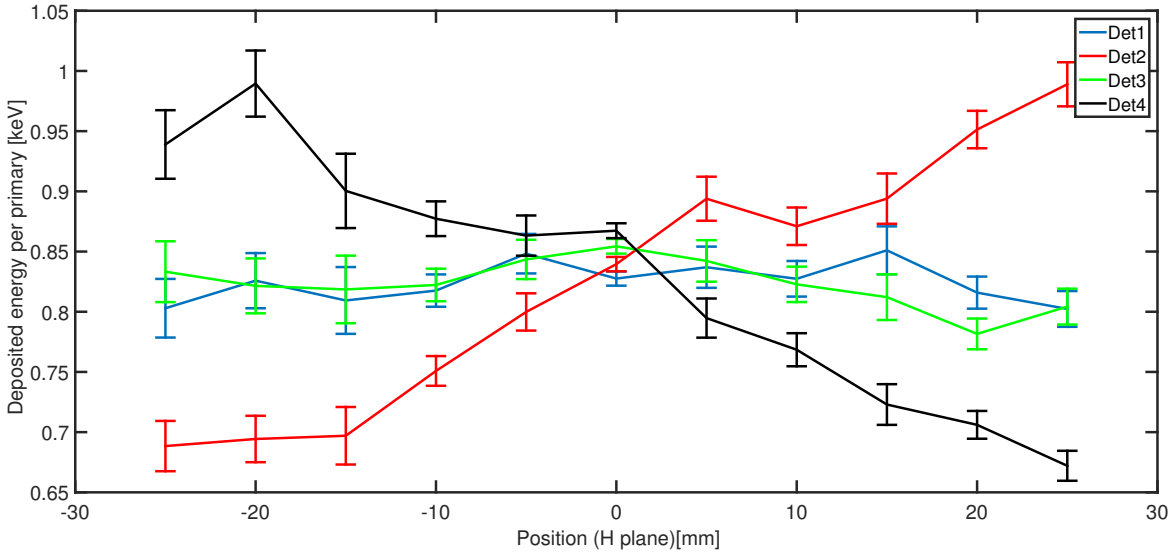


Figure 64: Energy deposited in each of the detectors at y=0 when the horizontal plane is scanned beam energy is 1000 MeV. Similar results are observed in the vertical plane with an inversion of the detector curves (i.e the flat curves are obtained with detector 2 and 4)

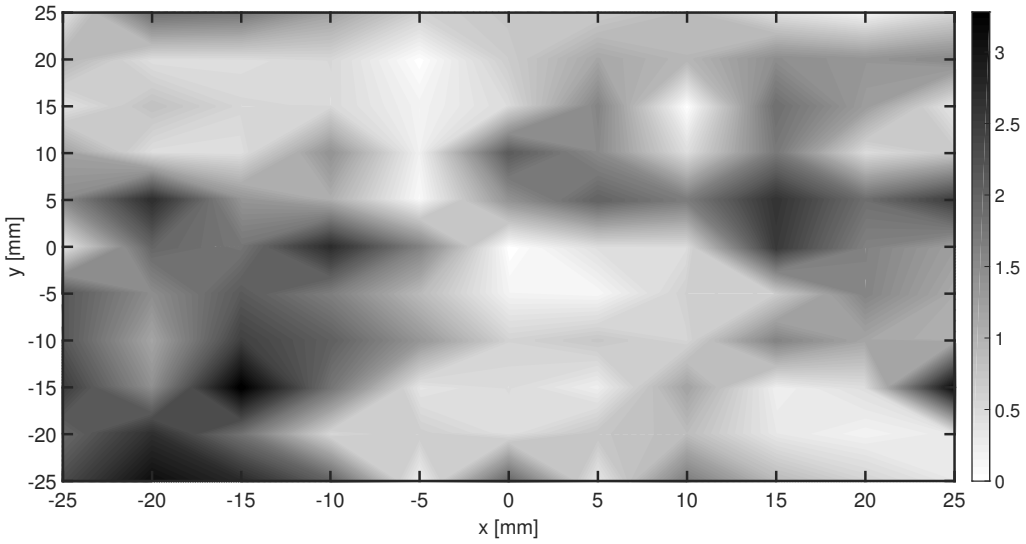


Figure 65: Absolute error map as function of the wire position, the beam energy is equal to 1300 MeV.

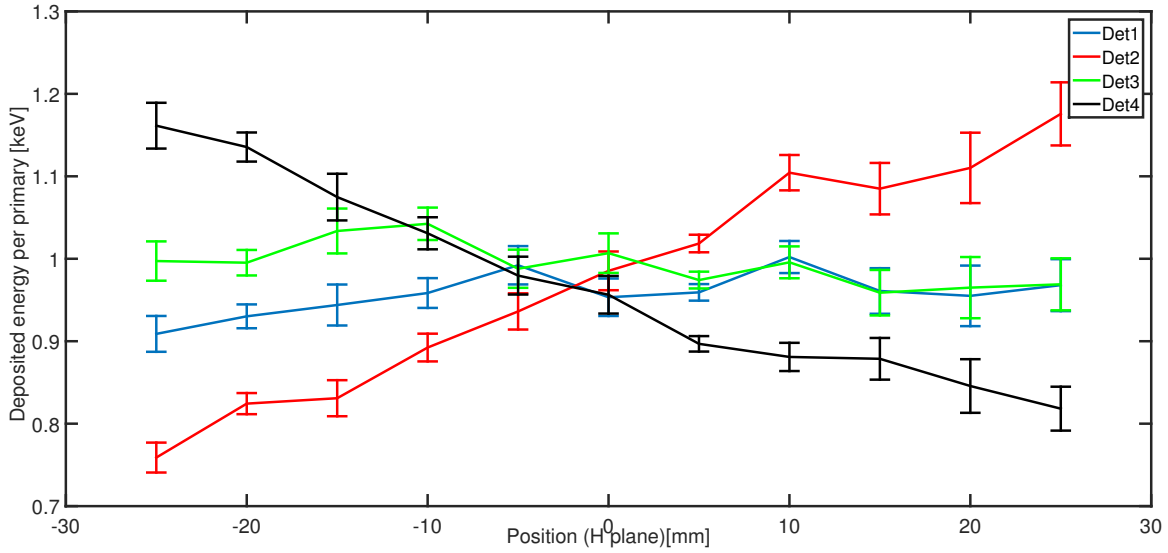


Figure 66: Energy deposited in each of the detectors at y=0 when the horizontal plane is scanned beam energy is 1300 MeV. Similar results are observed in the vertical plane with an inversion of the detector curves (i.e the flat curves are obtained with detector 2 and 4)

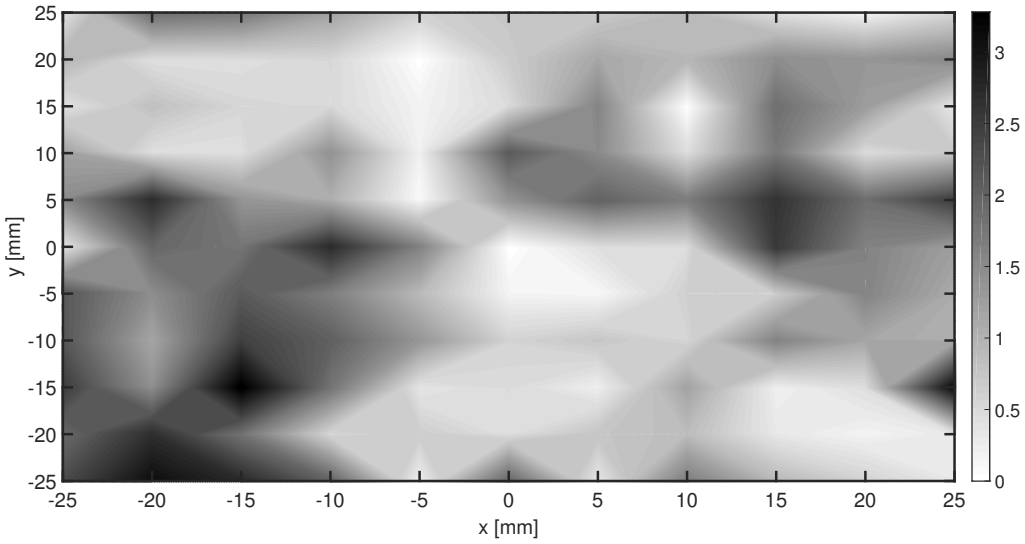


Figure 67: Absolute error map as function of the wire position, the beam energy is equal to 1300 MeV.

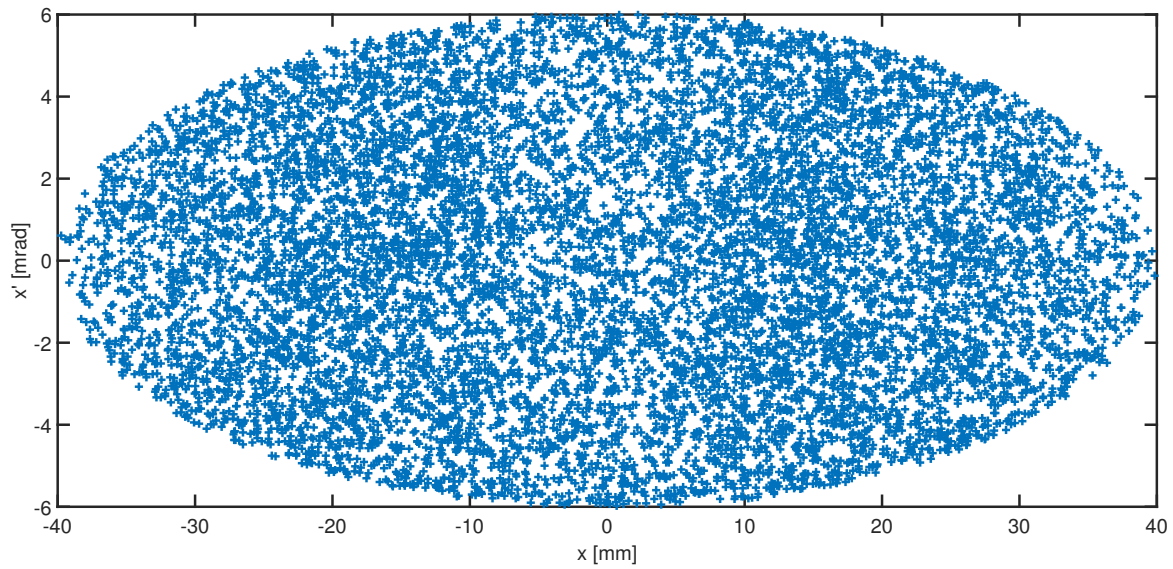


Figure 68: Distribution of the particles in the phase space for the "20sig." case (beam energy is 200 MeV) .

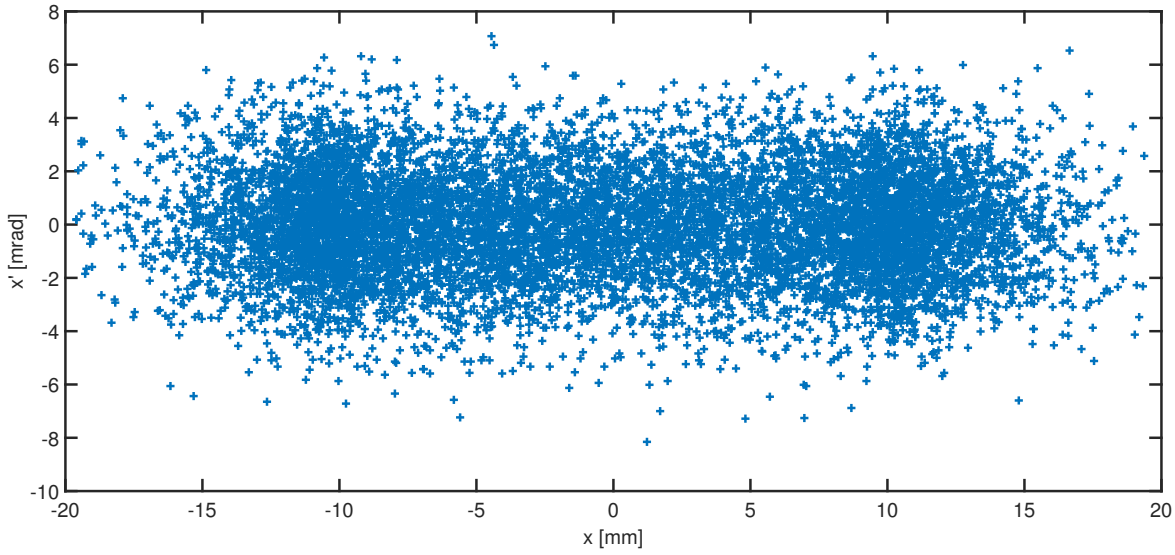


Figure 69: Distribution of the particles in the phase space for the "10sig. gauss" case (beam energy is 200 MeV).

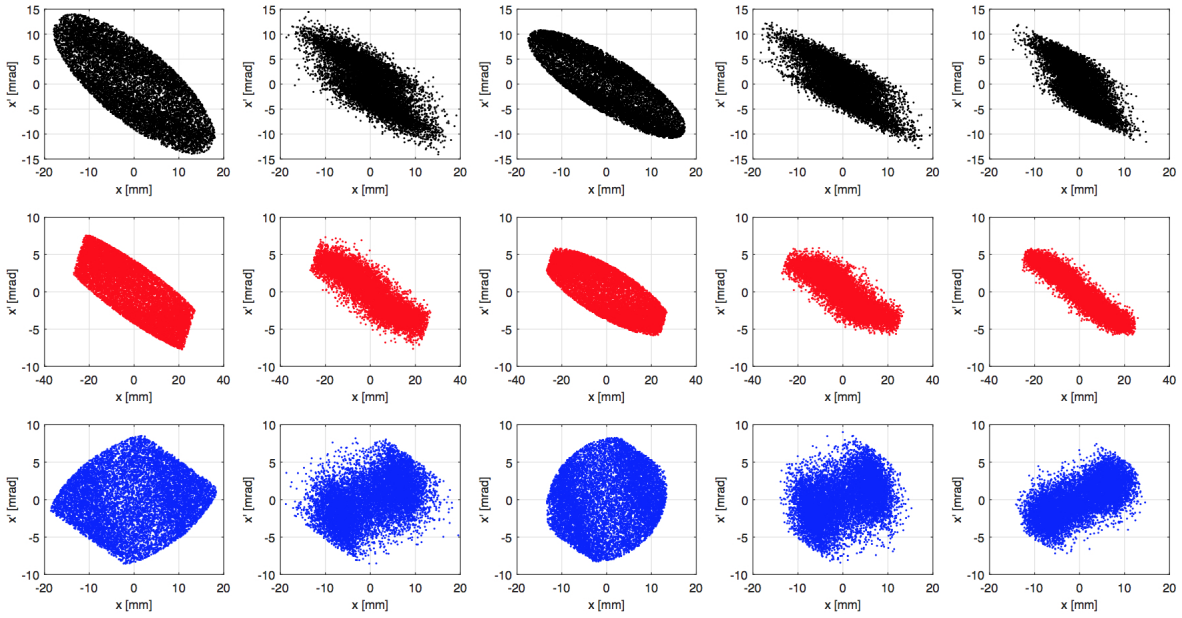


Figure 70: Evolution of the horizontal beam emittance along the 3 elliptical cells for the 5 particle sources considered in the simulation. At the exit of the first cell, the emittance is repented in black, in red at the exit of the sec on cell and in blue at the exit of the last cell. The first column is representing the beam source "15 sig. flat", the second, the beam source "15 sig. gauss", the third, the beam source "10 sig. flat", the fourth, the beam source "10 sig. gauss" and the last column the beam source "nominal".

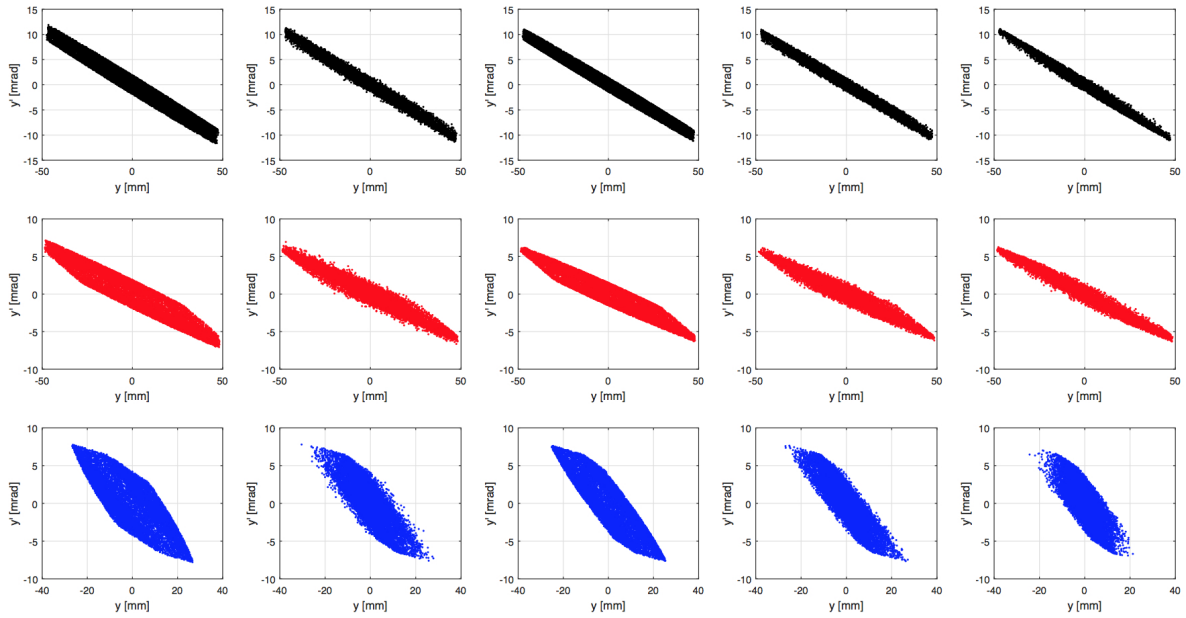


Figure 71: Evolution of the vertical beam emittance along the 3 elliptical cells for the 5 particle sources considered in the simulation. At the exit of the first cell, the emittance is repented in black, in red at the exit of the sec on cell and in blue at the exit of the last cell. The first column is representing the beam source "15 sig. flat", the second, the beam source "15 sig. gauss", the third, the beam source "10 sig. flat", the fourth, the beam source "10 sig. gauss" and the last column the beam source "nominal".